Electronic Research Archive

http://www.aimspress.com/journal/era

ERA, 34(10): 7330–7361.
DOI: 10.3934/era.2026317
Received: 18 June 2026
Revised: 06 August 2026
Accepted: 17 August 2026
Published: 26 August 2026

Research article

Tensor finite-time convergent gradient neural network for periodic Sylvester tensor equations with robotic applications

Mengyan Xie[1] **and Yang Zhang**[2,*]

[1] College of Information Technology, Shanghai Ocean University, Shanghai 201306, China
[2] Department of Mathematics, University of Manitoba, Winnipeg, MB, Canada

* **Correspondence:** Email: Yang.Zhang@umanitoba.ca.

Abstract: The periodic Sylvester tensor equation (PSTE) arises in multidimensional periodic systems. This paper proposes a tensor finite-time convergent gradient neural network (Tensor-FTCGNN) with a global adaptive gain for solving a class of PSTEs. Using the Einstein product, the periodically coupled tensor equations are formulated as a unified linear operator equation on a product tensor space, and the corresponding adjoint operator and global gradient are derived. Tensor linear operator theory and Lyapunov analysis are employed to establish the global finite-time convergence of the ideal continuous-time model and to derive an explicit upper bound for its settling time. For practical numerical implementation, a regularized Tensor-FTCGNN is introduced, which reaches an ϵ-dependent high-accuracy region in finite time and subsequently converges exponentially to the exact solution. Numerical experiments compare the proposed regularized model with representative gradient neural network (GNN) models, verify the theoretical finite-time upper bound through the observed Phase-I entrance times, and evaluate its convergence behavior over the tested tensor sizes. Finally, the proposed framework is applied to cooperative periodic trajectory reconstruction for a multiarm robotic system, illustrating its potential for multidimensional robotic applications.

Keywords: periodic Sylvester tensor equation; Einstein product; tensor operator; finite-time convergence; gradient neural network; multiarm robotic systems

1. Introduction

Recent studies have extended Sylvester- and Lyapunov-type equations to matrix, tensor, and quaternion settings. He et al. [1] investigated systems of Sylvester-like matrix equations over the quaternion algebra, and He et al. [2] developed a quaternion singular value decomposition (QSVD) method for multiple coupled Sylvester-type quaternion matrix equations. Li et al. [3] studied numerical algorithms for the discrete Lyapunov tensor equation, Wang et al. [4] investigated

least-squares solutions of the quaternion Sylvester tensor equation, and Xie et al. [5] developed a biconjugate gradient (BiCG) algorithm for generalized Sylvester tensor equations over the quaternions. For periodic matrix equations, Lv et al. [6] developed gradient-based neural networks for periodic Sylvester matrix equations, and Li and Ma [7] proposed an improved gradient neural network (GNN) model for the same class of problems. Wu et al. [8] developed an iterative algorithm for discrete periodic Lyapunov matrix equations. Bittanti and Colaneri [9] provided a systematic treatment of periodic systems, filtering, and control, and Hara et al. [10] studied repetitive control for periodic exogenous signals.

Structured numerical methods for tensor equations and related algebraic problems have received increasing attention in multidimensional computation. Kolda and Bader [11] provided a comprehensive treatment of tensor decompositions and their applications. Li and Wang [12] investigated a structure-preserving quaternion biconjugate gradient method. Xie et al. [13] proposed a fixed-time tensor gradient gradient neural network (TGNN) for the Sylvester tensor equation. More recently, Xue et al. [14] developed a tensor convolution-like low-rank dictionary for high-dimensional data representation.

Recent neurodynamic methods have also been extended to various tensor equations. Qi et al. [15] developed a finite-time zeroing neural network (ZNN) for the time-varying Lyapunov tensor equation, Mo et al. [16] considered the time-varying tensor square-root equation, and Li et al. [17] studied neural network solutions of polynomial systems with time-varying tensors. Xiao et al. [18] investigated a time-varying algebraic tensor Riccati equation, whereas Xie et al. [19] considered time-varying generalized Sylvester matrix equations. For finite-time neural dynamics, Zhang et al. [20] developed a robust finite-time GNN for time-varying systems of linear equations. Related gradient neural dynamics for linear matrix equations were studied by Petković et al. [21], Dakić and Petković [22], and Stanimirović and Petković [23]. These studies remain in the matrix setting, whereas the present work addresses periodically coupled higher-order Sylvester tensor equations through a combined tensor operator and its adjoint. However, the direct application of existing neurodynamic approaches to the periodic Sylvester tensor equation (PSTE) remains nontrivial. In particular, the cyclic coupling among multiple higher-order tensor states requires a unified tensor operator formulation. Moreover, establishing finite-time convergence without relying on element-wise discontinuous sign-like activation functions remains an important theoretical issue, and a numerically regularized implementation must also balance convergence acceleration and numerical robustness.

Motivated by the aforementioned issues, this paper investigates a class of discrete periodic Sylvester tensor equations using a neurodynamic framework. The main contributions are summarized as follows:

- **Tensor operator formulation:** The periodically coupled Sylvester equations are formulated to higher-order tensor spaces using the Einstein product. A combined periodic tensor operator and its adjoint are established on a product tensor space, providing a unified formulation of the residual and gradient.
- **Tensor-FTCGNN design:** An ideal continuous-time tensor finite-time convergent gradient neural network (Tensor-FTCGNN) equipped with a global adaptive gain is proposed without employing elementwise discontinuous sign activation functions. Its global finite-time convergence to the exact solution is established under the unique-solvability condition. For numerical implementation, a regularized model is further introduced, which reaches an ϵ-dependent high-accuracy region in finite time and then converges exponentially to the exact

solution.

- **Convergence analysis and numerical verification:** Using tensor linear operator theory and Lyapunov stability, an explicit upper bound for the settling time of the ideal model is derived. Numerical experiments compare the proposed regularized model with representative GNN models and verify the theoretical upper bound through the observed Phase-I entrance times.
- **Dimension-dependent numerical analysis and robotic application:** Numerical experiments investigate the convergence behavior of the proposed regularized model as the tested tensor size increases. In addition, cooperative periodic trajectory reconstruction for a multiarm robotic system is formulated within the PSTE framework, illustrating the potential applicability of the proposed method.

The rest of this paper is organized as follows. Section 2 introduces the necessary tensor-algebra preliminaries, formulates the PSTE through a combined periodic tensor operator, and discusses its solvability and numerical conditioning. Section 3 develops the ideal and regularized Tensor-FTCGNN models, establishes their respective convergence properties, and presents the corresponding computational algorithm. Section 4 provides comparative and dimension-dependent numerical experiments, verifies the Phase-I entrance time bound, and demonstrates cooperative periodic trajectory reconstruction for a multiarm robotic system together with a sampling interval sensitivity analysis. Finally, Section 5 concludes the paper and outlines directions for future research.

2. Preliminaries

This section briefly reviews the core notations of tensor algebra and the fundamental operations of the Einstein product, and it presents the mathematical description of the discrete periodic Sylvester tensor equations (PSTEs) investigated in this paper. Furthermore, a fundamental lemma regarding finite-time stability is introduced for the subsequent convergence analysis.

2.1. Notations and tensor operations

In this paper, $\mathbb{R}$ denotes the set of real numbers. Scalars are represented by lowercase letters (e.g., γ, p), matrices by uppercase letters (e.g., $\boldsymbol{A}, \boldsymbol{B}$), and higher-order tensors by calligraphic uppercase letters (e.g., $\mathcal{A}, \mathcal{X}$).

Definition 2.1 (Einstein product [24])**.** *Let tensor $\mathcal{A} \in \mathbb{R}^{I_1\times\cdots\times I_P\times K_1\times\cdots\times K_N}$ and tensor $\mathcal{B} \in \mathbb{R}^{K_1\times\cdots\times K_N\times J_1\times\cdots\times J_Q}$. The Einstein product of $\mathcal{A}$ and $\mathcal{B}$ along N modes is denoted by $\mathcal{A} *_N \mathcal{B} \in \mathbb{R}^{I_1\times\cdots\times I_P\times J_1\times\cdots\times J_Q}$, and its entries are defined as*

$$(\mathcal{A} *_N \mathcal{B})_{i_1\ldots i_P, j_1\ldots j_Q} = \sum_{k_1=1}^{K_1}\cdots\sum_{k_N=1}^{K_N} a_{i_1\ldots i_P, k_1\ldots k_N} b_{k_1\ldots k_N, j_1\ldots j_Q}. \tag{2.1}$$

The Einstein product is a natural generalization of matrix multiplication in higher-order tensor spaces and satisfies both associativity and distributivity.

Definition 2.2 (Tensor transpose and inner product)**.** *To accommodate the operation rules of the Einstein product, for a tensor $\mathcal{A} \in \mathbb{R}^{I_1\times\cdots\times I_P\times K_1\times\cdots\times K_N}$, its generalized transpose is defined as*

$\mathcal{A}^\top \in \mathbb{R}^{K_1\times\cdots\times K_N\times I_1\times\cdots\times I_P}$. *It can be proven that the Einstein product satisfies the following transpose property:*

$$(\mathcal{A} *_N \mathcal{B})^\top = \mathcal{B}^\top *_N \mathcal{A}^\top. \tag{2.2}$$

The standard inner product of two tensors $\mathcal{X}, \mathcal{Y} \in \mathbb{R}^{I_1\times\cdots\times I_P}$ of the same dimensions is defined as the sum of the products of all their corresponding elements, denoted by $\langle \mathcal{X}, \mathcal{Y}\rangle$. The tensor Frobenius norm induced by this inner product is given by $\|\mathcal{X}\|_F = \sqrt{\langle \mathcal{X}, \mathcal{X}\rangle}$.

2.2. Problem formulation

This paper concerns the solution of a class of discrete (PSTEs) featuring multistage coupling characteristics, which effectively extends conventional periodic matrix equations [6] into higher-order tensor spaces. Consider a discrete-time system with a period $T \in \mathbb{N}^+$. For any arbitrary stage $j \in \{0, 1, \ldots, T-1\}$, the corresponding tensor equation is formulated as

$$\mathcal{A}_j *_N \mathcal{X}_j + \mathcal{X}_{j+1} *_M \mathcal{B}_j = \mathcal{C}_j, \tag{2.3}$$

where $\mathcal{A}_j$, $\mathcal{B}_j$, and $\mathcal{C}_j$ are prescribed stage-dependent tensors that are treated as constant within stage j, and $\mathcal{X}_j$ is the unknown state tensor. To accommodate the inherent periodicity of the system, the state tensors are subject to the following cyclic boundary condition:

$$\mathcal{X}_T = \mathcal{X}_0.$$

2.3. Combined periodic tensor operator and its adjoint

To reveal the global algebraic structure of the periodically coupled tensor equations, we formulate the PSTE as a single linear equation defined on a product tensor space.

Let

$$\mathbb{X} = \mathbb{R}^{I_1\times\cdots\times I_N\times J_1\times\cdots\times J_M} \tag{2.4}$$

denote the state tensor space. For each $j \in \{0, 1, \ldots, T-1\}$, the dimensions and roles of the principal tensor variables are summarized in Table 1.

Table 1. Dimensions and roles of the principal tensor variables.

Symbol	Tensor space	Role
$\mathcal{X}_j$	$\mathbb{R}^{I_1\times\cdots\times I_N\times J_1\times\cdots\times J_M}$	Unknown state tensor
$\mathcal{C}_j$	$\mathbb{R}^{I_1\times\cdots\times I_N\times J_1\times\cdots\times J_M}$	Target tensor
$\mathcal{A}_j$	$\mathbb{R}^{I_1\times\cdots\times I_N\times I_1\times\cdots\times I_N}$	Left coefficient tensor
$\mathcal{B}_j$	$\mathbb{R}^{J_1\times\cdots\times J_M\times J_1\times\cdots\times J_M}$	Right coefficient tensor

Accordingly, the Einstein products $\mathcal{A}_j *_N \mathcal{X}_j$ and $\mathcal{X}_{j+1} *_M \mathcal{B}_j$ are both well-defined and belong to $\mathbb{X}$. Define the product tensor space

$$\mathbb{H} = \prod_{j=0}^{T-1} \mathbb{X},$$

whose elements are represented by $\boldsymbol{\mathcal{X}} = (\mathcal{X}_0, \mathcal{X}_1, \ldots, \mathcal{X}_{T-1})$. For any $\boldsymbol{\mathcal{X}}, \boldsymbol{\mathcal{Y}} \in \mathbb{H}$, define the product-space inner product as

$$\langle \boldsymbol{\mathcal{X}}, \boldsymbol{\mathcal{Y}} \rangle_{\mathbb{H}} = \sum_{j=0}^{T-1} \left\langle \mathcal{X}_j, \mathcal{Y}_j \right\rangle_F \tag{2.5}$$

and the corresponding norm as $\|\boldsymbol{\mathcal{X}}\|_{\mathbb{H}}^2 = \sum_{j=0}^{T-1} \left\|\mathcal{X}_j\right\|_F^2$.

Definition 2.3 (Combined periodic tensor operator)**.** *Define the linear operator*

$$\mathscr{L} : \mathbb{H} \to \mathbb{H} \tag{2.6}$$

by $(\mathscr{L}\boldsymbol{\mathcal{X}})_j = \mathcal{A}_j *_N \mathcal{X}_j + \mathcal{X}_{j+1} *_M \mathcal{B}_j$, $j = 0, 1, \ldots, T-1$, *where all stage indices are interpreted modulo* T*, namely,* $\mathcal{X}_T = \mathcal{X}_0$.

By introducing the stacked target tensor

$$\boldsymbol{\mathcal{C}} = (\mathcal{C}_0, \mathcal{C}_1, \ldots, \mathcal{C}_{T-1}),$$

the PSTE in (2.3) together with the periodic boundary condition can be written compactly as

$$\mathscr{L}\boldsymbol{\mathcal{X}} = \boldsymbol{\mathcal{C}}.$$

Proposition 2.4 (Adjoint of the combined periodic tensor operator)**.** *With respect to the inner product defined in* (2.5)*, the adjoint operator*

$$\mathscr{L}^* : \mathbb{H} \to \mathbb{H} \tag{2.7}$$

is given by

$$(\mathscr{L}^*\boldsymbol{\mathcal{Y}})_j = \mathcal{A}_j^\top *_N \mathcal{Y}_j + \mathcal{Y}_{j-1} *_M \mathcal{B}_{j-1}^\top, \qquad j = 0, 1, \ldots, T-1, \tag{2.8}$$

where the indices are interpreted modulo T*, that is,*

$$\mathcal{Y}_{-1} = \mathcal{Y}_{T-1}, \qquad \mathcal{B}_{-1} = \mathcal{B}_{T-1}.$$

Proof. For arbitrary $\boldsymbol{\mathcal{X}}, \boldsymbol{\mathcal{Y}} \in \mathbb{H}$, the definition of $\mathscr{L}$ gives

$$\langle \mathscr{L}\boldsymbol{\mathcal{X}}, \boldsymbol{\mathcal{Y}} \rangle_{\mathbb{H}} = \sum_{j=0}^{T-1} \left\langle \mathcal{A}_j *_N \mathcal{X}_j, \mathcal{Y}_j \right\rangle_F + \sum_{j=0}^{T-1} \left\langle \mathcal{X}_{j+1} *_M \mathcal{B}_j, \mathcal{Y}_j \right\rangle_F. \tag{2.9}$$

Using the adjoint properties of the Einstein product, we have

$$\left\langle \mathcal{A}_j *_N \mathcal{X}_j, \mathcal{Y}_j \right\rangle_F = \left\langle \mathcal{X}_j, \mathcal{A}_j^\top *_N \mathcal{Y}_j \right\rangle_F$$

and

$$\left\langle \mathcal{X}_{j+1} *_M \mathcal{B}_j, \mathcal{Y}_j \right\rangle_F = \left\langle \mathcal{X}_{j+1}, \mathcal{Y}_j *_M \mathcal{B}_j^\top \right\rangle_F.$$

Reindexing the second summation in (2.9) according to the periodic convention yields

$$\sum_{j=0}^{T-1} \left\langle \mathcal{X}_{j+1}, \mathcal{Y}_j *_M \mathcal{B}_j^\top \right\rangle_F = \sum_{j=0}^{T-1} \left\langle \mathcal{X}_j, \mathcal{Y}_{j-1} *_M \mathcal{B}_{j-1}^\top \right\rangle_F.$$

Therefore,

$$\langle \mathscr{L}\boldsymbol{\mathcal{X}}, \boldsymbol{\mathcal{Y}} \rangle_{\mathbb{H}} = \sum_{j=0}^{T-1} \left\langle \mathcal{X}_j, \mathcal{A}_j^\top *_N \mathcal{Y}_j + \mathcal{Y}_{j-1} *_M \mathcal{B}_{j-1}^\top \right\rangle_F \langle \boldsymbol{\mathcal{X}}, \mathscr{L}^*\boldsymbol{\mathcal{Y}} \rangle_{\mathbb{H}}. \tag{2.10}$$

This proves (2.8). □

2.4. Solvability and practical verification

Assume that the coefficient tensors $\mathcal{B}_j$, $j = 0, 1, \ldots, T-1$, are nonsingular under the Einstein product $*_M$. Define the forward monodromy tensors as

$$\mathbf{\Phi}_{\boldsymbol{A}} = \mathcal{A}_{T-1} *_N \mathcal{A}_{T-2} *_N \cdots *_N \mathcal{A}_0,$$

and

$$\mathbf{\Phi}_{\boldsymbol{B}} = \mathcal{B}_{T-1} *_M \mathcal{B}_{T-2} *_M \cdots *_M \mathcal{B}_0.$$

To derive the unique solvability condition, consider the homogeneous PSTE

$$\mathcal{A}_j *_N \mathcal{Z}_j + \mathcal{Z}_{j+1} *_M \mathcal{B}_j = \mathcal{O}, \qquad j = 0, 1, \ldots, T-1,$$

subject to $\mathcal{Z}_T = \mathcal{Z}_0$. Because $\mathcal{B}_j$ is nonsingular,

$$\mathcal{Z}_{j+1} = -\mathcal{A}_j *_N \mathcal{Z}_j *_M \mathcal{B}_j^{-1}.$$

Repeated substitution gives, for $k = 1, \ldots, T$,

$$\mathcal{Z}_k = (-1)^k \left(\mathcal{A}_{k-1} *_N \cdots *_N \mathcal{A}_0\right) *_N \mathcal{Z}_0 *_M \left(\mathcal{B}_0^{-1} *_M \cdots *_M \mathcal{B}_{k-1}^{-1}\right).$$

In particular,

$$\mathcal{Z}_T = (-1)^T \mathbf{\Phi}_{\boldsymbol{A}} *_N \mathcal{Z}_0 *_M \mathbf{\Phi}_{\boldsymbol{B}}^{-1},$$

where the inverse of the right monodromy tensor is

$$\mathbf{\Phi}_{\boldsymbol{B}}^{-1} = \mathcal{B}_0^{-1} *_M \mathcal{B}_1^{-1} *_M \cdots *_M \mathcal{B}_{T-1}^{-1}.$$

Using the periodic condition $\mathcal{Z}_T = \mathcal{Z}_0$ and multiplying from the right by $\mathbf{\Phi}_B$ yields

$$\mathbf{\Phi}_{\boldsymbol{A}} *_N \mathcal{Z}_0 - (-1)^T \mathcal{Z}_0 *_M \mathbf{\Phi}_B = \mathcal{O}.$$

This is a homogeneous Sylvester tensor equation. Under the matrix representation induced by the Einstein product, it has only the trivial solution if and only if the spectra of $\mathbf{\Phi}_A$ and $(-1)^T \mathbf{\Phi}_B$ are disjoint. Therefore, the PSTE has a unique solution for every $\mathcal{C} \in \mathbb{H}$ if and only if

$$\sigma(\mathbf{\Phi}_{\boldsymbol{A}}) \cap (-1)^T \sigma(\mathbf{\Phi}_{\boldsymbol{B}}) = \varnothing, \tag{2.11}$$

where $\sigma(\cdot)$ denotes the spectrum of the corresponding tensor operator. Under Condition (2.11), the homogeneous PSTE admits only the trivial solution. In terms of the combined periodic operator introduced in Section 2.3, this property is equivalently written as

$$\ker(\mathscr{L}) = \{\mathcal{O}_{\mathbb{H}}\}. \tag{2.12}$$

Because $\mathscr{L} : \mathbb{H} \to \mathbb{H}$ is a linear operator on a finite-dimensional space, injectivity is equivalent to bijectivity. Hence, $\mathscr{L}$ is invertible, and $\mathscr{L}\mathcal{X} = \mathcal{C}$ admits a unique solution for every $\mathcal{C} \in \mathbb{H}$. Furthermore, for every $\mathcal{Z} \in \mathbb{H}$,

$$\langle \mathcal{Z}, \mathscr{L}^* \mathscr{L} \mathcal{Z} \rangle_{\mathbb{H}} = \|\mathscr{L} \mathcal{Z}\|_{\mathbb{H}}^2. \tag{2.13}$$

Define the normal operator

$$\mathscr{H} := \mathscr{L}^* \mathscr{L}. \tag{2.14}$$

Therefore, under Condition (12), $\mathscr{H}$ is positive definite. The detailed spectral bounds associated with this operator are established in Lemma 3.1.

Remark 2.5 (Numerical verification of solvability)**.** Under a Frobenius norm-preserving vectorization of the product tensor space, let

$$d = \left(\prod_{r=1}^{N} I_r\right)\left(\prod_{s=1}^{M} J_s\right),$$

and define the matrix representations $\mathbf{L}_{\boldsymbol{A}_j}, \mathbf{R}_{\boldsymbol{B}_j} \in \mathbb{R}^{d\times d}$ by $\mathbf{L}_{\boldsymbol{A}_j}\operatorname{vec}(\mathcal{Z}) = \operatorname{vec}\left(\mathcal{A}_j *_N \mathcal{Z}\right)$, and $\mathbf{R}_{\boldsymbol{B}_j}\operatorname{vec}(\mathcal{Z}) = \operatorname{vec}\left(\mathcal{Z} *_M \mathcal{B}_j\right)$. Then, the combined operator $\mathscr{L}$ admits the block-cyclic matrix representation

$$\mathscr{L}_{\text{mat}} = \begin{bmatrix} \mathbf{L}_{\boldsymbol{A}_0} & \mathbf{R}_{\boldsymbol{B}_0} & 0 & \cdots & 0 \\ 0 & \mathbf{L}_{\boldsymbol{A}_1} & \mathbf{R}_{\boldsymbol{B}_1} & \cdots & 0 \\ \vdots & & \ddots & \ddots & \vdots \\ 0 & \cdots & 0 & \mathbf{L}_{\boldsymbol{A}_{T-2}} & \mathbf{R}_{\boldsymbol{B}_{T-2}} \\ \mathbf{R}_{\boldsymbol{B}_{T-1}} & 0 & \cdots & 0 & \mathbf{L}_{\boldsymbol{A}_{T-1}} \end{bmatrix}$$

such that

$$\mathscr{L}_{\text{mat}}\mathbf{x} = \mathbf{c},$$

where

$$\mathbf{x} = \begin{bmatrix} \operatorname{vec}(\mathcal{X}_0) \\ \vdots \\ \operatorname{vec}(\mathcal{X}_{T-1}) \end{bmatrix}, \qquad \mathbf{c} = \begin{bmatrix} \operatorname{vec}(C_0) \\ \vdots \\ \operatorname{vec}(C_{T-1}) \end{bmatrix}.$$

The exact unique-solvability condition is equivalently expressed as

$$\sigma_{\min}\left(\mathscr{L}_{\text{mat}}\right) > 0,$$

where $\sigma_{\min}(\cdot)$ denotes the minimum singular value.

In finite-precision computation, the numerical well-posedness of the PSTE can be assessed using

$$\sigma_{\min}\left(\mathscr{L}_{\text{mat}}\right) > \delta_{\text{sol}},$$

where $\delta_{\text{sol}} > 0$ is a prescribed numerical threshold. If $\sigma_{\min}(\mathscr{L}_{\text{mat}})$ is positive but close to zero, the PSTE remains theoretically solvable but is numerically ill-conditioned.

The associated operator condition number is $\kappa_{\mathscr{L}} = \sigma_{\max}(\mathscr{L}_{\text{mat}})/\sigma_{\min}(\mathscr{L}_{\text{mat}}) = \sqrt{\lambda_{\max}/\lambda_{\min}}$, where $\lambda_{\min} = \lambda_{\min}\left(\mathscr{L}^*\mathscr{L}\right)$, $\lambda_{\max} = \lambda_{\max}\left(\mathscr{L}^*\mathscr{L}\right)$. A large value of $\kappa_{\mathscr{L}}$ indicates high sensitivity of the PSTE solution to perturbations in the coefficient and target tensors.

Remark 2.6 (Online conditioning monitoring for varying coefficients)**.** For practical extensions in which the coefficient tensors vary with time or operating conditions, denote the corresponding combined operator by $\mathscr{L}(t)$. Its numerical well-posedness can be monitored by periodically estimating $\widehat{\sigma}_{\min}(\mathscr{L}_{\text{mat}}(t))$ or, equivalently, $\widehat{\lambda}_{\min}(\mathscr{L}^*(t)\mathscr{L}(t))$, where the hat denotes a numerical estimate of the corresponding extremal spectral quantity.

For moderate-scale systems, the minimum singular value can be computed using a standard singular-value decomposition. For large-scale tensor systems, a full block matrix need not be constructed explicitly. Instead, matrix-free iterative singular-value estimation can be performed using only the operator actions $\mathscr{L}(t)\boldsymbol{\mathcal{Z}}$ and $\mathscr{L}(t)^*\boldsymbol{\mathcal{Y}}$.

A conditioning warning may be activated when $\widehat{\sigma}_{\min}\left(\mathscr{L}_{\text{mat}}(t)\right) \le \delta_{\text{warn}}$, where δ_{warn} is selected according to the required solution accuracy and the expected magnitude of coefficient perturbations.

Remark 2.7 (Remedial strategy for an ill-conditioned PSTE)**.** If the combined operator becomes singular or severely ill-conditioned, a Tikhonov-regularized least-squares formulation can be considered:

$$\min_{\mathcal{X}\in\mathbb{H}} \frac{1}{2}\|\mathscr{L}\mathcal{X}-\mathcal{C}\|_{\mathbb{H}}^2+\frac{\rho}{2}\|\mathcal{X}\|_{\mathbb{H}}^2, \qquad \rho>0.$$

The gradient of the regularized objective is $\mathcal{G}_\rho = \mathscr{L}^*(\mathscr{L}\mathcal{X}-\mathcal{C})+\rho\mathcal{X}$. The corresponding regularized normal operator becomes $\mathscr{H}_\rho = \mathscr{L}^*\mathscr{L}+\rho\mathscr{I}$ and satisfies $\lambda_{\min}\left(\mathscr{H}_\rho\right)\geq\rho>0$.

This regularization improves numerical robustness, but the resulting state generally represents a stable approximate solution rather than the exact solution of the original singular PSTE. In robotic applications, other remedial actions include reducing the sampling interval, updating the local Jacobian linearization, increasing the damping level, or employing a truncated pseudoinverse solver.

In the remainder of this paper, we focus on the uniquely solvable case satisfying

$$\lambda_{\min}(\mathscr{L}^*\mathscr{L})>0.$$

The regularized formulation in Remark 2.7 is presented as a practical remedial strategy and is not included in the finite-time convergence analysis of the exact PSTE solution.

2.5. Finite-time stability lemma

To rigorously prove the finite-time convergence of the proposed neural network model in subsequent sections, we introduce a fundamental lemma from Lyapunov finite-time stability theory, which has been widely utilized in neurodynamic computing and finite-time control systems [25, 26].

Lemma 2.8 (Finite-time stability [25, 26])**.** Consider the autonomous system

$$\dot{\boldsymbol{x}}(t)=\boldsymbol{f}(\boldsymbol{x}(t)), \qquad \boldsymbol{f}(\mathbf{0})=\mathbf{0}.$$

Assume that, for every initial state, a unique forward-complete solution exists under the adopted solution concept. Suppose that there exists a continuously differentiable, positive definite, and radially unbounded function

$$V:\mathbb{R}^d\to\mathbb{R}_{\geq 0}$$

such that

$$\dot{V}(\boldsymbol{x}(t))\leq -cV(\boldsymbol{x}(t))^\alpha$$

for almost every t satisfying $\boldsymbol{x}(t)\neq\mathbf{0}$, where $c>0$, and $\alpha\in(0,1)$. Then, the origin is globally finite-time stable, and the settling time satisfies

$$T(\boldsymbol{x}_0)\leq\frac{V(\boldsymbol{x}_0)^{1-\alpha}}{c(1-\alpha)}.$$

3. Main results

This section develops the Tensor-FTCGNN for solving the PSTE. We first formulate an ideal continuous-time model and establish its global finite-time convergence to the exact solution under the unique solvability condition. We then introduce a regularized model for numerical implementation and prove its dual-phase convergence, consisting of finite-time entrance into an ϵ-dependent high-accuracy region followed by exponential refinement.

3.1. Development of the Tensor-FTCGNN model

Define the stacked residual tensor as

$$\mathcal{E} = (\mathcal{E}_0, \mathcal{E}_1, \ldots, \mathcal{E}_{T-1}) = \mathscr{L}\mathcal{X} - \mathcal{C}.$$

The global energy function can be expressed compactly as

$$J(\mathcal{X}) = \frac{1}{2} \|\mathscr{L}\mathcal{X} - \mathcal{C}\|_{\mathbb{H}}^2 = \frac{1}{2} \|\mathcal{E}\|_{\mathbb{H}}^2 .$$

For any perturbation $\mathcal{Z} \in \mathbb{H}$, the directional derivative of $J(\mathcal{X})$ is

$$DJ(\mathcal{X})[\mathcal{Z}] = \langle \mathscr{L}\mathcal{X} - \mathcal{C}, \mathscr{L}\mathcal{Z} \rangle_{\mathbb{H}} \langle \mathscr{L}^* (\mathscr{L}\mathcal{X} - \mathcal{C}), \mathcal{Z} \rangle_{\mathbb{H}} .$$

It follows that the global gradient is

$$\mathcal{G} = \nabla J(\mathcal{X}) = \mathscr{L}^* (\mathscr{L}\mathcal{X} - \mathcal{C}) = \mathscr{L}^* \mathcal{E}.$$

According to Proposition 2.4, the jth component of the global gradient is

$$\mathcal{G}_j = \mathcal{A}_j^\top *_N \mathcal{E}_j + \mathcal{E}_{j-1} *_M \mathcal{B}_{j-1}^\top, \qquad j = 0, 1, \ldots, T-1. \tag{3.1}$$

Let

$$\Omega(t) = \|\mathcal{G}(t)\|_{\mathbb{H}}^2 = \sum_{k=0}^{T-1} \|\mathcal{G}_k(t)\|_F^2 .$$

The ideal continuous-time Tensor-FTCGNN is designed as

$$\dot{\mathcal{X}}(t) = \begin{cases} -\gamma \dfrac{\mathcal{G}(t)}{\Omega(t)^{p/2}}, & \Omega(t) > 0, \\ \mathbf{0}, & \Omega(t) = 0, \end{cases} \tag{3.2}$$

where $\gamma > 0$ is the convergence-rate parameter, and $p \in (0, 1]$ is the finite-time acceleration exponent.

For $0 < p < 1$, the vector field in (3.2) extends continuously to the equilibrium through the zero branch. For $p = 1$, a solution of (3.2) is defined as an absolutely continuous trajectory $\mathcal{X} : [0, \infty) \to \mathbb{H}$ satisfying the differential equation almost everywhere whenever $\Omega(t) > 0$. If

$$t_c := \inf\{t \geq 0 : \Omega(t) = 0\} < \infty,$$

the trajectory is continued by

$$\mathcal{X}(t) = \mathcal{X}(t_c), \qquad t \geq t_c,$$

or equivalently, by $\dot{\mathcal{X}}(t) = 0$ after t_c. Because the vector field is locally Lipschitz on the open set $\{\mathcal{X} \in \mathbb{H} : \Omega(\mathcal{X}) > 0\}$, the solution exists uniquely in the classical sense before reaching the equilibrium. Under the unique solvability condition, let $\mathcal{X}^*$ denote the exact PSTE solution, and define the stacked solution error as

$$\widetilde{\mathcal{X}} = \mathcal{X} - \mathcal{X}^*.$$

Moreover, for $0 < p \le 1$ and $\Omega(t) > 0$,

$$\|\dot{\boldsymbol{\mathcal{X}}}(t)\|_{\mathbb{H}} = \gamma \|\boldsymbol{\mathcal{G}}(t)\|_{\mathbb{H}}^{1-p} \le \gamma \|\mathcal{H}\|_{\mathrm{op}}^{1-p} \|\widetilde{\boldsymbol{\mathcal{X}}}\|_{\mathbb{H}}^{1-p},$$

where $\|\mathcal{H}\|_{\mathrm{op}}$ denotes the operator norm induced by $\|\cdot\|_{\mathbb{H}}$. Hence, the vector field has at most sublinear growth, and no finite escape can occur. Together with local uniqueness before the hitting time and the prescribed zero continuation, this gives a unique forward-complete trajectory under the adopted solution concept. Equivalently, when $\Omega(t) > 0$, the jth state tensor satisfies

$$\dot{\mathcal{X}}_j(t) = -\gamma \frac{\mathcal{G}_j(t)}{\left(\sum_{k=0}^{T-1} \|\mathcal{G}_k(t)\|_F^2\right)^{p/2}}, \qquad j = 0, 1, \ldots, T-1.$$

Because $\mathscr{L}\boldsymbol{\mathcal{X}}^* = \boldsymbol{\mathcal{C}}$, we have $\boldsymbol{\mathcal{E}} = \mathscr{L}\widetilde{\boldsymbol{\mathcal{X}}}$, $\boldsymbol{\mathcal{G}} = \mathscr{H}\widetilde{\boldsymbol{\mathcal{X}}}$. Because $\mathscr{H}$ is positive definite, one has $\Omega(t) = 0 \Longleftrightarrow \widetilde{\boldsymbol{\mathcal{X}}}(t) = \mathbf{0}$. Therefore, the second branch in (3.2) defines the exact solution as an equilibrium of the ideal dynamics.

3.2. Global finite-time convergence of the ideal model

Before presenting the finite-time convergence theorem, we establish the spectral bounds of the combined periodic tensor operator.

Lemma 3.1 (Spectral norm bounds of the combined operator)**.** Suppose that the unique solvability condition in Section 2.4 is satisfied. Then the normal operator $\mathscr{H} = \mathscr{L}^*\mathscr{L}$ is self-adjoint and positive definite on $\mathbb{H}$. Let $\lambda_{\min} = \lambda_{\min}(\mathscr{H}) > 0$, $\lambda_{\max} = \lambda_{\max}(\mathscr{H})$. For every $\boldsymbol{\mathcal{Z}} \in \mathbb{H}$, the following inequalities hold:

$$\lambda_{\min} \|\boldsymbol{\mathcal{Z}}\|_{\mathbb{H}}^2 \le \|\mathscr{L}\boldsymbol{\mathcal{Z}}\|_{\mathbb{H}}^2 \le \lambda_{\max} \|\boldsymbol{\mathcal{Z}}\|_{\mathbb{H}}^2, \tag{3.3}$$

and

$$\lambda_{\min}^2 \|\boldsymbol{\mathcal{Z}}\|_{\mathbb{H}}^2 \le \|\mathscr{L}^*\mathscr{L}\boldsymbol{\mathcal{Z}}\|_{\mathbb{H}}^2 \le \lambda_{\max}^2 \|\boldsymbol{\mathcal{Z}}\|_{\mathbb{H}}^2. \tag{3.4}$$

Furthermore,

$$\lambda_{\min} \|\mathscr{L}\boldsymbol{\mathcal{Z}}\|_{\mathbb{H}}^2 \le \|\mathscr{L}^*\mathscr{L}\boldsymbol{\mathcal{Z}}\|_{\mathbb{H}}^2 \le \lambda_{\max} \|\mathscr{L}\boldsymbol{\mathcal{Z}}\|_{\mathbb{H}}^2. \tag{3.5}$$

Proof. By Section 2.4, $\mathscr{H}$ is positive definite. It remains to note that, for arbitrary $\boldsymbol{\mathcal{Z}}, \boldsymbol{\mathcal{Y}} \in \mathbb{H}$, the definition $\mathscr{H} = \mathscr{L}^*\mathscr{L}$ and the adjoint relation give

$$\langle \boldsymbol{\mathcal{Z}}, \mathscr{H}\boldsymbol{\mathcal{Y}} \rangle_{\mathbb{H}} = \langle \boldsymbol{\mathcal{Z}}, \mathscr{L}^*\mathscr{L}\boldsymbol{\mathcal{Y}} \rangle_{\mathbb{H}} = \langle \mathscr{L}\boldsymbol{\mathcal{Z}}, \mathscr{L}\boldsymbol{\mathcal{Y}} \rangle_{\mathbb{H}} = \langle \mathscr{L}^*\mathscr{L}\boldsymbol{\mathcal{Z}}, \boldsymbol{\mathcal{Y}} \rangle_{\mathbb{H}} = \langle \mathscr{H}\boldsymbol{\mathcal{Z}}, \boldsymbol{\mathcal{Y}} \rangle_{\mathbb{H}}.$$

Hence, $\mathscr{H}$ is self-adjoint.

Because $\mathbb{H}$ is a finite-dimensional inner-product space, and $\mathscr{H}$ is self-adjoint and positive definite, the spectral theorem guarantees the existence of an orthonormal eigenbasis of $\mathbb{H}$, and all eigenvalues of $\mathscr{H}$ are real and strictly positive. Thus, for every nonzero $\boldsymbol{\mathcal{Z}} \in \mathbb{H}$, the Rayleigh quotient satisfies

$$\lambda_{\min} \le \frac{\langle \boldsymbol{\mathcal{Z}}, \mathscr{H}\boldsymbol{\mathcal{Z}} \rangle_{\mathbb{H}}}{\|\boldsymbol{\mathcal{Z}}\|_{\mathbb{H}}^2} \le \lambda_{\max}. \tag{3.6}$$

Using (2.13) in (3.6) yields (3.3).

In addition, $\|\mathscr{H}\mathcal{Z}\|_{\mathbb{H}}^2 = \langle \mathscr{H}\mathcal{Z}, \mathscr{H}\mathcal{Z}\rangle_{\mathbb{H}} = \left\langle \mathcal{Z}, \mathscr{H}^2\mathcal{Z}\right\rangle_{\mathbb{H}}$. The smallest and largest eigenvalues of $\mathscr{H}^2$ are $\lambda_{\min}^2$ and $\lambda_{\max}^2$, respectively. Applying the Rayleigh quotient to $\mathscr{H}^2$ proves (3.4).

Finally, let $\{\boldsymbol{\mathcal{U}}_r\}$ be an orthonormal eigenbasis of $\mathscr{H}$ with $\mathscr{H}\boldsymbol{\mathcal{U}}_r = \lambda_r\boldsymbol{\mathcal{U}}_r$, and write $\mathcal{Z} = \sum_r z_r\boldsymbol{\mathcal{U}}_r$. Then, $\|\mathscr{L}\mathcal{Z}\|_{\mathbb{H}}^2 = \sum_r \lambda_r|z_r|^2$, and $\|\mathscr{H}\mathcal{Z}\|_{\mathbb{H}}^2 = \sum_r \lambda_r^2|z_r|^2$. Because $\lambda_{\min}\lambda_r \le \lambda_r^2 \le \lambda_{\max}\lambda_r$, inequality (3.5) follows. □

Applying Lemma 3.1 gives

$$\lambda_{\min}\sum_{j=0}^{T-1}\left\|\widetilde{\mathcal{X}}_j\right\|_F^2 \le \sum_{j=0}^{T-1}\left\|\mathcal{E}_j\right\|_F^2 \le \lambda_{\max}\sum_{j=0}^{T-1}\left\|\widetilde{\mathcal{X}}_j\right\|_F^2$$

and

$$\lambda_{\min}^2\sum_{j=0}^{T-1}\left\|\widetilde{\mathcal{X}}_j\right\|_F^2 \le \sum_{j=0}^{T-1}\left\|\mathcal{G}_j\right\|_F^2 \le \lambda_{\max}^2\sum_{j=0}^{T-1}\left\|\widetilde{\mathcal{X}}_j\right\|_F^2.$$

The operator formulation also yields the following identity:

$$\left\langle\widetilde{\boldsymbol{\mathcal{X}}}, \boldsymbol{\mathcal{G}}\right\rangle_{\mathbb{H}} = \left\langle\widetilde{\boldsymbol{\mathcal{X}}}, \mathscr{L}^*\mathscr{L}\widetilde{\boldsymbol{\mathcal{X}}}\right\rangle_{\mathbb{H}} = \left\langle\mathscr{L}\widetilde{\boldsymbol{\mathcal{X}}}, \mathscr{L}\widetilde{\boldsymbol{\mathcal{X}}}\right\rangle_{\mathbb{H}} = \|\boldsymbol{\mathcal{E}}\|_{\mathbb{H}}^2. \tag{3.7}$$

Equivalently, $\sum_{j=0}^{T-1}\left\langle\widetilde{\mathcal{X}}_j, \mathcal{G}_j\right\rangle_F = \sum_{j=0}^{T-1}\left\|\mathcal{E}_j\right\|_F^2$.

Theorem 3.2 (Global finite-time convergence of the ideal model)**.** Suppose that the PSTE admits a unique solution $\boldsymbol{\mathcal{X}}^*$, or equivalently, $\ker(\mathscr{L}) = \{\mathbf{0}_{\mathbb{H}}\}$. Let the model parameters satisfy $\gamma > 0$, $p \in (0, 1]$. Then, starting from any initial state $\boldsymbol{\mathcal{X}}(0) \in \mathbb{H}$, the ideal Tensor-FTCGNN (3.2) converges globally to the exact solution $\boldsymbol{\mathcal{X}}^*$ within a finite settling time t_c.

Moreover, the settling time satisfies

$$t_c \le \frac{\lambda_{\max}^p}{p\gamma\lambda_{\min}}\left\|\widetilde{\boldsymbol{\mathcal{X}}}(0)\right\|_{\mathbb{H}}^p, \tag{3.8}$$

where $\widetilde{\boldsymbol{\mathcal{X}}}(0) = \boldsymbol{\mathcal{X}}(0) - \boldsymbol{\mathcal{X}}^*$. Equivalently, the bound can be expressed in terms of the initial residual as

$$t_c \le \frac{\lambda_{\max}^p}{p\gamma\lambda_{\min}^{1+p/2}}\|\boldsymbol{\mathcal{E}}(0)\|_{\mathbb{H}}^p. \tag{3.9}$$

Proof. Define the stacked solution error as $\widetilde{\boldsymbol{\mathcal{X}}}(t) = \boldsymbol{\mathcal{X}}(t) - \boldsymbol{\mathcal{X}}^*$. Consider the Lyapunov function

$$V(t) = \frac{1}{2}\left\|\widetilde{\boldsymbol{\mathcal{X}}}(t)\right\|_{\mathbb{H}}^2 = \frac{1}{2}\sum_{j=0}^{T-1}\left\|\widetilde{\mathcal{X}}_j(t)\right\|_F^2. \tag{3.10}$$

Clearly, $V(t)$ is positive definite and radially unbounded with respect to $\widetilde{\boldsymbol{\mathcal{X}}}(t)$. When $\Omega(t) > 0$, differentiating (3.10) along the trajectory of (3.2) gives

$$\dot{V}(t) = \left\langle\widetilde{\boldsymbol{\mathcal{X}}}(t), \dot{\boldsymbol{\mathcal{X}}}(t)\right\rangle_{\mathbb{H}} = -\gamma\frac{\left\langle\widetilde{\boldsymbol{\mathcal{X}}}(t), \boldsymbol{\mathcal{G}}(t)\right\rangle_{\mathbb{H}}}{\Omega(t)^{p/2}}.$$

According to (3.7), $\left\langle \widetilde{\boldsymbol{\mathcal{X}}}(t), \boldsymbol{\mathcal{G}}(t) \right\rangle_{\mathbb{H}} = \|\boldsymbol{\mathcal{E}}(t)\|_{\mathbb{H}}^2$. Therefore,

$$\dot{V}(t) = -\gamma \frac{\|\boldsymbol{\mathcal{E}}(t)\|_{\mathbb{H}}^2}{\|\boldsymbol{\mathcal{G}}(t)\|_{\mathbb{H}}^p}. \tag{3.11}$$

By Lemma 3.1,

$$\|\boldsymbol{\mathcal{E}}(t)\|_{\mathbb{H}}^2 \geq \lambda_{\min} \left\|\widetilde{\boldsymbol{\mathcal{X}}}(t)\right\|_{\mathbb{H}}^2, \tag{3.12}$$

and

$$\|\boldsymbol{\mathcal{G}}(t)\|_{\mathbb{H}}^2 \leq \lambda_{\max}^2 \left\|\widetilde{\boldsymbol{\mathcal{X}}}(t)\right\|_{\mathbb{H}}^2.$$

Consequently,

$$\|\boldsymbol{\mathcal{G}}(t)\|_{\mathbb{H}}^p \leq \lambda_{\max}^p \left\|\widetilde{\boldsymbol{\mathcal{X}}}(t)\right\|_{\mathbb{H}}^p. \tag{3.13}$$

Substituting (3.12) and (3.13) into (3.11) yields

$$\dot{V}(t) \leq -\gamma \frac{\lambda_{\min} \left\|\widetilde{\boldsymbol{\mathcal{X}}}(t)\right\|_{\mathbb{H}}^2}{\lambda_{\max}^p \left\|\widetilde{\boldsymbol{\mathcal{X}}}(t)\right\|_{\mathbb{H}}^p} = -\gamma \frac{\lambda_{\min}}{\lambda_{\max}^p} \left\|\widetilde{\boldsymbol{\mathcal{X}}}(t)\right\|_{\mathbb{H}}^{2-p}.$$

Using $\left\|\widetilde{\boldsymbol{\mathcal{X}}}(t)\right\|_{\mathbb{H}}^2 = 2V(t)$, we obtain $\dot{V}(t) \leq -\beta V(t)^\alpha$, where $\alpha = 1 - p/2 \in [1/2, 1)$, and

$$\beta = \gamma \frac{\lambda_{\min}}{\lambda_{\max}^p} 2^{1-p/2} > 0. \tag{3.14}$$

The above differential inequality holds on the interval where $\Omega(t) > 0$. For $p = 1$, the inequality holds almost everywhere along the absolutely continuous solution defined after (3.2). Once $\Omega(t) = 0$ is reached, the prescribed zero continuation keeps the trajectory at the exact equilibrium. The Lyapunov function in (3.10) is continuously differentiable, positive definite, and radially unbounded with respect to $\mathcal{X}_e$. Together with the solution interpretation and the zero continuation specified after (3.2), the hypotheses of Lemma 2.8 are satisfied.

By the finite-time stability lemma, $V(t)$ reaches zero within a finite time satisfying

$$t_c \leq \frac{V(0)^{1-\alpha}}{\beta(1-\alpha)}. \tag{3.15}$$

Since $1 - \alpha = p/2$, substitution of (3.14) and $V(0) = 1/2 \left\|\widetilde{\boldsymbol{\mathcal{X}}}(0)\right\|_{\mathbb{H}}^2$ into (3.15) gives $t_c \leq \lambda_{\max}^p \left\|\widetilde{\boldsymbol{\mathcal{X}}}(0)\right\|_{\mathbb{H}}^p / (p\gamma\lambda_{\min})$, which proves (3.8).

Finally, from (3.3), $\lambda_{\min} \left\|\widetilde{\boldsymbol{\mathcal{X}}}(0)\right\|_{\mathbb{H}}^2 \leq \|\boldsymbol{\mathcal{E}}(0)\|_{\mathbb{H}}^2$. Hence, $\left\|\widetilde{\boldsymbol{\mathcal{X}}}(0)\right\|_{\mathbb{H}}^p \leq \lambda_{\min}^{-p/2} \|\boldsymbol{\mathcal{E}}(0)\|_{\mathbb{H}}^p$. Combining this inequality with (3.8) yields (3.9). Therefore, the ideal Tensor-FTCGNN globally converges to the exact PSTE solution within a finite time. □

Remark 3.3 (Scope of the finite-time convergence theorem)**.** Theorem 3.2 concerns the ideal continuous-time dynamics (3.2), in which the adaptive denominator is exactly $\Omega(t)^{p/2}$ whenever $\Omega(t) > 0$. The parameter range of the ideal model is restricted to $0 < p \leq 1$, with the limiting case

$p = 1$ interpreted in the absolutely continuous sense specified after (3.2). The numerical threshold ϵ used in the practical digital implementation is not included in this theorem.

When the denominator is replaced by

$$\max\left\{\Omega(t)^{p/2}, \epsilon\right\},$$

the resulting regularized dynamics retain the ideal finite-time behavior before entering an ϵ-dependent accuracy region, but exhibit exponential convergence inside that region. The regularized model is analyzed separately in the following subsection.

Remark 3.4 (Singular-value interpretation of the spectral bounds)**.** Using the block-cyclic matrix representation $\mathscr{L}_{\text{mat}}$ introduced in Remark 2.5, the normal operator $\mathscr{H} = \mathscr{L}^*\mathscr{L}$ is represented by

$$\mathscr{H}_{\text{mat}} = \mathscr{L}_{\text{mat}}^{\top}\mathscr{L}_{\text{mat}}.$$

Consequently,

$$\lambda_{\min} = \sigma_{\min}^2(\mathscr{L}_{\text{mat}}), \qquad \lambda_{\max} = \sigma_{\max}^2(\mathscr{L}_{\text{mat}}).$$

Thus, the spectral bounds in Lemma 3.1 admit a direct singular-value interpretation.

3.3. Regularized numerical implementation and dual-phase convergence

Although the ideal continuous-time model in (3.2) possesses exact finite-time convergence, the denominator $\Omega(t)^{p/2}$ approaches zero as the solution is reached. In a digital implementation, this may produce an excessively large effective gain or a division-by-zero operation. To improve numerical robustness, we introduce a small regularization parameter $\epsilon > 0$ and consider the following regularized dynamics:

$$\dot{\boldsymbol{\mathcal{X}}}(t) = -\gamma\frac{\boldsymbol{\mathcal{G}}(t)}{\max\left\{\Omega(t)^{p/2}, \epsilon\right\}}, \tag{3.16}$$

where $\Omega(t) = \|\boldsymbol{\mathcal{G}}(t)\|_{\mathbb{H}}^2$.

Define the ϵ-dependent region $\mathcal{D}_\epsilon = \left\{\boldsymbol{\mathcal{X}} \in \mathbb{H} \;\middle|\; \|\boldsymbol{\mathcal{G}}(\boldsymbol{\mathcal{X}})\|_{\mathbb{H}}^p \le \epsilon\right\}$. The switching time between the two dynamic phases is defined as

$$t_\epsilon = \inf\left\{t \ge 0 \;\middle|\; \Omega(t)^{p/2} \le \epsilon\right\}.$$

If the initial state already belongs to $\mathcal{D}_\epsilon$, we set $t_\epsilon = 0$. Accordingly, we refer to the evolution before entering $\mathcal{D}_\epsilon$, that is, $0 \le t < t_\epsilon$, as **Phase I**, and the post-entry evolution for $t \ge t_\epsilon$ as **Phase II**. The positive invariance of $\mathcal{D}_\epsilon$ and the convergence properties of these two phases are established in the following Proposition.

Proposition 3.5 (Dual-phase convergence of the regularized model)**.** Suppose that the PSTE admits a unique solution $\boldsymbol{\mathcal{X}}^*$ and that $\gamma > 0$, $p \in (0, 2)$, and $\epsilon > 0$. Then, the regularized Tensor-FTCGNN (3.16) has the following properties.

(1). If $\boldsymbol{\mathcal{X}}(0) \notin \mathcal{D}_\epsilon$, the trajectory reaches $\mathcal{D}_\epsilon$ within a finite time t_ϵ.

(2). At the switching time and throughout the second phase, the solution error and residual satisfy

$$\left\|\widetilde{\boldsymbol{\mathcal{X}}}(t)\right\|_{\mathbb{H}} \le \frac{\epsilon^{1/p}}{\lambda_{\min}}, \qquad t \ge t_\epsilon, \tag{3.17}$$

and

$$\|\mathcal{E}(t)\|_{\mathbb{H}} \leq \frac{\sqrt{\lambda_{\max}}}{\lambda_{\min}}\epsilon^{1/p}, \qquad t \geq t_\epsilon. \tag{3.18}$$

(3). Once the trajectory enters $\mathcal{D}_\epsilon$, this region is positively invariant, and the solution error converges exponentially to zero:

$$V(t) \leq V(t_\epsilon)\exp\left[-\frac{2\gamma\lambda_{\min}}{\epsilon}(t-t_\epsilon)\right], \qquad t \geq t_\epsilon. \tag{3.19}$$

Moreover, the finite switching time satisfies

$$t_\epsilon \leq \frac{V(0)^{1-\alpha_\epsilon} - V(t_\epsilon)^{1-\alpha_\epsilon}}{\beta(1-\alpha_\epsilon)} \leq \frac{\lambda_{\max}^p}{p\gamma\lambda_{\min}}\left\|\widetilde{\boldsymbol{\mathcal{X}}}(0)\right\|_{\mathbb{H}}^p,$$

where $\alpha_\epsilon = 1 - p/2, \beta = \gamma 2^{1-p/2}\lambda_{\min}/\lambda_{\max}^p$.

Proof. When $\mathcal{X}(t) \in \mathbb{H} \setminus \mathcal{D}_\epsilon$, one has $\Omega(t)^{p/2} > \epsilon$. Hence, the regularized dynamics have the same form as the ideal dynamics, and

$$\dot{V}(t) \leq -\beta V(t)^{\alpha_\epsilon}, \qquad \alpha_\epsilon = 1 - \frac{p}{2} \in (0,1), \tag{3.20}$$

where

$$\beta = \gamma 2^{1-p/2}\lambda_{\min}/\lambda_{\max}^p.$$

We first show that the trajectory enters $\mathcal{D}_\epsilon$ in finite time. Suppose, by contradiction, that

$$\mathcal{X}(t) \notin \mathcal{D}_\epsilon \qquad \text{for all } t \geq 0.$$

Then, (3.20) holds for all $t \geq 0$, and integration over $[0, t]$ gives

$$V(t)^{1-\alpha_\epsilon} \leq V(0)^{1-\alpha_\epsilon} - \beta(1-\alpha_\epsilon)t. \tag{3.21}$$

For $t > V(0)^{1-\alpha_\epsilon}/\beta(1-\alpha_\epsilon)$, the right-hand side of (3.21) is negative, which contradicts $V(t) \geq 0$. Therefore, the entrance set is nonempty and $t_\epsilon < \infty$.

Because the trajectory is continuous, and $\mathcal{D}_\epsilon$ is closed, $\mathcal{X}(t_\epsilon) \in \mathcal{D}_\epsilon$. Applying (3.21) for $0 \leq t < t_\epsilon$ and letting $t \to t_\epsilon$ yields

$$t_\epsilon \leq \frac{V(0)^{1-\alpha_\epsilon} - V(t_\epsilon)^{1-\alpha_\epsilon}}{\beta(1-\alpha_\epsilon)} \leq \frac{V(0)^{1-\alpha_\epsilon}}{\beta(1-\alpha_\epsilon)}.$$

Using $V(0) = 1/2\|\mathcal{X}_e(0)\|_{\mathbb{H}}^2$ gives

$$t_\epsilon \leq \frac{\lambda_{\max}^p}{p\gamma\lambda_{\min}}\|\mathcal{X}_e(0)\|_{\mathbb{H}}^p.$$

At $t = t_\epsilon$, the definition of $\mathcal{D}_\epsilon$ yields $\|\mathcal{G}(t_\epsilon)\|_{\mathbb{H}}^p = \Omega(t_\epsilon)^{p/2} \leq \epsilon$. Equivalently,

$$\|\mathcal{G}(t_\epsilon)\|_{\mathbb{H}} \leq \epsilon^{1/p}. \tag{3.22}$$

According to Lemma 3.1,

$$\|\mathcal{G}\|_{\mathbb{H}} = \left\|\mathscr{H}\widetilde{\boldsymbol{\mathcal{X}}}\right\|_{\mathbb{H}} \geq \lambda_{\min}\left\|\widetilde{\boldsymbol{\mathcal{X}}}\right\|_{\mathbb{H}}. \tag{3.23}$$

Combining (3.22) and (3.23) gives $\left\|\widetilde{\boldsymbol{\mathcal{X}}}(t_\epsilon)\right\|_{\mathbb{H}} \leq \epsilon^{1/p}/\lambda_{\min}$. Furthermore, by (3.3), $\|\boldsymbol{\mathcal{E}}(t_\epsilon)\|_{\mathbb{H}} \leq \sqrt{\lambda_{\max}}\left\|\widetilde{\boldsymbol{\mathcal{X}}}(t_\epsilon)\right\|_{\mathbb{H}}$, which yields $\|\boldsymbol{\mathcal{E}}(t_\epsilon)\|_{\mathbb{H}} \leq \sqrt{\lambda_{\max}}\epsilon^{1/p}/\lambda_{\min}$.

We next prove that $\mathcal{D}_\epsilon$ is positively invariant. Suppose, by contradiction, that the trajectory leaves $\mathcal{D}_\epsilon$ after t_ϵ. Define the first exit time as

$$t_{\text{out}} = \inf\{t > t_\epsilon \mid \boldsymbol{\mathcal{X}}(t) \notin \mathcal{D}_\epsilon\}.$$

By the continuity of the trajectory and of $\Omega(t)$, one has $\Omega(t)^{p/2} \leq \epsilon$, $t \in [t_\epsilon, t_{\text{out}}]$, and $\Omega(t_{\text{out}})^{p/2} = \epsilon$. Therefore, on $[t_\epsilon, t_{\text{out}}]$, the denominator in (3.16) is equal to ϵ, and

$$\dot{\widetilde{\boldsymbol{\mathcal{X}}}}(t) = -\frac{\gamma}{\epsilon}\mathscr{H}\widetilde{\boldsymbol{\mathcal{X}}}(t). \tag{3.24}$$

Because $\boldsymbol{\mathcal{G}} = \mathscr{H}\widetilde{\boldsymbol{\mathcal{X}}}$, it follows that

$$\dot{\Omega}(t) = 2\left\langle \boldsymbol{\mathcal{G}}(t), \dot{\boldsymbol{\mathcal{G}}}(t)\right\rangle_{\mathbb{H}} = 2\left\langle \mathscr{H}\widetilde{\boldsymbol{\mathcal{X}}}(t), \mathscr{H}\dot{\widetilde{\boldsymbol{\mathcal{X}}}}(t)\right\rangle_{\mathbb{H}} = -\frac{2\gamma}{\epsilon}\left\langle \mathscr{H}\widetilde{\boldsymbol{\mathcal{X}}}(t), \mathscr{H}^2\widetilde{\boldsymbol{\mathcal{X}}}(t)\right\rangle_{\mathbb{H}} \leq 0.$$

Indeed, if $\widetilde{\boldsymbol{\mathcal{X}}} = \sum_r z_r \boldsymbol{\mathcal{U}}_r$ is expanded in an orthonormal eigenbasis of $\mathscr{H}$, then

$$\left\langle \mathscr{H}\widetilde{\boldsymbol{\mathcal{X}}}, \mathscr{H}^2\widetilde{\boldsymbol{\mathcal{X}}}\right\rangle_{\mathbb{H}} = \sum_r \lambda_r^3 |z_r|^2 \geq 0.$$

Moreover, at the boundary $\Omega^{p/2} = \epsilon > 0$, this quantity is strictly positive. Hence, $\dot{\Omega}(t_{\text{out}}) < 0$, which is incompatible with an outward first exit from $\mathcal{D}_\epsilon$. This contradiction proves that t_{out} does not exist. Therefore, $\mathcal{D}_\epsilon$ is positively invariant.

Consequently, for every $t \geq t_\epsilon$, the denominator in (3.16) remains equal to ϵ, and the Phase II dynamics are given by (3.24). The time derivative of the Lyapunov function satisfies

$$\dot{V}(t) = -\frac{\gamma}{\epsilon}\left\langle \widetilde{\boldsymbol{\mathcal{X}}}(t), \mathscr{H}\widetilde{\boldsymbol{\mathcal{X}}}(t)\right\rangle_{\mathbb{H}} = -\frac{\gamma}{\epsilon}\|\boldsymbol{\mathcal{E}}(t)\|_{\mathbb{H}}^2 \leq -\frac{2\gamma\lambda_{\min}}{\epsilon}V(t).$$

Applying the comparison lemma yields (3.19). Because $\mathcal{D}_\epsilon$ is positively invariant, (3.17) and (3.18) remain valid for all $t \geq t_\epsilon$. □

The above result characterizes the convergence of the regularized Tensor-FTCGNN as a two-phase process. The trajectory first reaches the ϵ-dependent region $\mathcal{D}_\epsilon$ within a finite time and subsequently converges exponentially to the exact PSTE solution. Moreover, the derived state-error and residual bounds scale as $\epsilon^{1/p}$. Therefore, the parameter ϵ determines the transition threshold between the finite-time reaching phase and the exponential refinement phase. A smaller ϵ yields tighter post-entry error bounds, although it may increase numerical stiffness in a discrete-time implementation.

Remark 3.6 (Step-size condition in the exponential refinement phase)**.** Consider the explicit Euler discretization of the regularized model with step size $\Delta t > 0$ and iteration index k. In Phase II, the error update is

$$\widetilde{\boldsymbol{\mathcal{X}}}^{(k+1)} = \left(\mathscr{I} - \frac{\gamma\Delta t}{\epsilon}\mathscr{H}\right)\widetilde{\boldsymbol{\mathcal{X}}}^{(k)},$$

where $\mathscr{I}$ denotes the identity operator on $\mathbb{H}$. Because the eigenvalues of $\mathscr{H}$ lie in $[\lambda_{\min}, \lambda_{\max}]$, the explicit Euler iteration is asymptotically stable if $0 < \gamma\Delta t/\epsilon < 2/\lambda_{\max}$. Equivalently,

$$0 < \Delta t < 2\epsilon/\gamma\lambda_{\max}. \tag{3.25}$$

Thus, decreasing ϵ while keeping Δt fixed may produce numerical oscillation or instability. A sufficiently small time step, an adaptive-step solver, or an implicit integration scheme should be employed when a very small value of ϵ is used. The condition in (3.25) characterizes the explicit Euler discretization of the Phase II linear dynamics; the numerical stability of the complete nonlinear transient should also be verified in practice.

3.4. Algorithm procedure

Algorithm 1: Regularized Tensor-FTCGNN for the PSTE

Input: $\{\mathcal{A}_j, \mathcal{B}_j, C_j\}$, γ, p, ϵ, Δt, tol, $K_{\max}$, and $\{\mathcal{X}_j^{(0)}\}$
Output: $\{\mathcal{X}_j\}$

$\|\mathcal{C}\|_{\mathbb{H}} \leftarrow \left(\sum_{j=0}^{T-1} \|C_j\|_F^2\right)^{1/2}$;
for $k = 0, \ldots, K_{\max} - 1$ **do**
  for $j = 0, \ldots, T-1$ **do**
    $j_+ \leftarrow (j+1) \bmod T$;
    $\mathcal{E}_j^{(k)} \leftarrow \mathcal{A}_j *_N \mathcal{X}_j^{(k)} + \mathcal{X}_{j_+}^{(k)} *_M \mathcal{B}_j - C_j$;
  end
  $r^{(k)} \leftarrow \|\mathcal{E}^{(k)}\|_{\mathbb{H}} / \max\{\|\mathcal{C}\|_{\mathbb{H}}, 1\}$;
  if $r^{(k)} \le$ tol **then**
    break;
  end
  for $j = 0, \ldots, T-1$ **do**
    $j_- \leftarrow (j-1+T) \bmod T$;
    $\mathcal{G}_j^{(k)} \leftarrow \mathcal{A}_j^\top *_N \mathcal{E}_j^{(k)} + \mathcal{E}_{j_-}^{(k)} *_M \mathcal{B}_{j_-}^\top$;
  end
  $\Omega^{(k)} \leftarrow \sum_{j=0}^{T-1} \|\mathcal{G}_j^{(k)}\|_F^2$;
  $d^{(k)} \leftarrow \max\{(\Omega^{(k)})^{p/2}, \epsilon\}$;
  for $j = 0, \ldots, T-1$ **do**
    $\mathcal{X}_j^{(k+1)} \leftarrow \mathcal{X}_j^{(k)} - (\gamma\Delta t/d^{(k)})\mathcal{G}_j^{(k)}$;
  end
end
if $r^{(k)} \le$ tol **then**
  return $\{\mathcal{X}_j^{(k)}\}_{j=0}^{T-1}$;
end
return $\{\mathcal{X}_j^{(K_{\max})}\}_{j=0}^{T-1}$;

For practical numerical implementation, the regularized Tensor-FTCGNN is discretized by the explicit Euler method, as summarized in Algorithm 1. The ideal model is retained as the theoretical counterpart for establishing the finite-time convergence properties. All residual and gradient tensors at the current iteration are computed before any state tensor is updated, thereby ensuring a synchronous periodic stage update.

The regularization parameter ϵ prevents a singular denominator and limits the effective numerical gain near the solution. When $(\Omega^{(k)})^{p/2} > \epsilon$, Algorithm 1 operates in the finite-time-accelerated branch corresponding to the ideal continuous-time dynamics. When $(\Omega^{(k)})^{p/2} \leq \epsilon$, it switches to a linear gradient-refinement phase. Subject to an appropriate discretization step size, the algorithm reproduces the two-phase numerical behavior of the regularized continuous-time model: accelerated residual reduction before the switching threshold, followed by linear gradient refinement.

The stopping tolerance tol is independent of the regularization parameter ϵ. The former specifies the desired numerical termination accuracy, whereas the latter determines the transition threshold between the two dynamic phases. In Algorithm 1, $K_{\max}$ denotes the maximum number of iterations. Accordingly, Theorem 3.2 applies to the ideal continuous-time model, whereas Algorithm 1 is an explicit Euler discretization of the regularized continuous-time model analyzed in Proposition 3.5. The stability of the discrete implementation additionally depends on the step-size condition in Remark 3.6.

4. Numerical experiments and application

This section evaluates the convergence behavior and numerical characteristics of the proposed regularized Tensor-FTCGNN. Section 4.1 compares the residual trajectories with representative GNN models. Section 4.2 examines the Phase I entrance time against the theoretical finite-time upper bound. Section 4.3 investigates the convergence behavior of the model across increasing tested tensor dimensions. Section 4.4 presents a multi arm robotic application involving cooperative periodic trajectory-reference reconstruction and investigates the sensitivity of the piecewise constant Jacobian approximation to the sampling interval.

All numerical experiments were conducted in MATLAB R2023b on a computer equipped with an Intel(R) Core(TM) i7-14700 CPU (2.10 GHz) and 32.0 GB RAM, running Windows 11. In the model comparison in Section 4, all continuous-time neurodynamic models were integrated using MATLAB `ode15s` with identical solver tolerances and the same output time grid. Solver-specific settings for the remaining experiments are provided in the corresponding subsections.

4.1. Numerical comparison of convergence behavior

In this first experiment, a fundamental numerical simulation is conducted for the PSTE. To evaluate the solution accuracy and convergence behavior, we prescribe the exact solutions as unit tensors, that is

$$\mathcal{X}_j^* = \mathbf{1}_{n\times n\times n}, \qquad j \in \{0, 1, 2, 3\}.$$

For the third-order numerical experiments, we set $N = 1$, $M = 2$, and $I_1 = J_1 = J_2 = n$. Therefore, $\mathcal{X}_j, \mathcal{C}_j \in \mathbb{R}^{n\times n\times n}$, $\mathcal{A}_j \in \mathbb{R}^{n\times n}$, and $\mathcal{B}_j \in \mathbb{R}^{n\times n\times n\times n}$. The left coefficient matrices $\mathcal{A}_j$ and the auxiliary matrices $\widehat{\boldsymbol{B}}_j \in \mathbb{R}^{n\times n}$ are generated with random entries in $(-1, 1)$. For efficient implementation, the

fourth-order right coefficient tensor $\mathcal{B}_j$ is represented implicitly through $\widehat{\boldsymbol{B}}_j$ as

$$(\mathcal{B}_j)_{abcd} = \delta_{ac}(\widehat{\boldsymbol{B}}_j)_{bd},$$

where δ_{ac} denotes the Kronecker delta. Consequently, the Einstein product $\mathcal{X}_{j+1} *_2 \mathcal{B}_j$ is exactly equivalent to the mode-3 matrix multiplication of $\mathcal{X}_{j+1}$ by $\widehat{\boldsymbol{B}}_j$ used in the numerical implementation. The corresponding target tensors $\{\mathcal{C}_j\}$ are constructed according to the PSTE. The tensor dimension is set to $n = 3$, and the number of periodic stages is $T = 4$. The common network gain is set to $\gamma = 10$, while the proposed regularized Tensor-FTCGNN uses $p = 1$ and $\epsilon = 10^{-4}$. All models use the same randomly generated initial tensor states and are integrated over $t \in [0, 2]$ using MATLAB `ode15s`, with RelTol $= 10^{-8}$, AbsTol $= 10^{-10}$, and MaxStep $= 10^{-2}$ s. A uniform output grid with spacing 2×10^{-3} s and random seed 42 are used.

To provide a scale-independent evaluation, the convergence curves are measured using the relative global residual

$$r_{\mathrm{rel}}(t) = \frac{\|\mathcal{E}(t)\|_{\mathbb{H}}}{\max\{\|\mathcal{C}\|_{\mathbb{H}}, 1\}}.$$

The convergence trajectories generated by the different models are depicted in Figure 1. For a comprehensive comparison, the proposed regularized Tensor-FTCGNN is evaluated against representative tensor GNN models. The linear, power, power-sigmoid, and sign-bi-power models are expressed in the general gradient-activation form

$$\dot{\mathcal{X}}_j(t) = -\gamma\Phi(\mathcal{G}_j(t)),$$

where $\Phi(\cdot)$ denotes an element wise tensor mapping induced by a scalar activation function $\phi(\cdot)$. The activation functions used in the simulation are listed below.

(1). Linear activation function: $\phi_{\mathrm{lin}}(x) = x$.

(2). Power activation function: $\phi_{\mathrm{pow}}(x) = \mathrm{sig}^{q_p}(x), q_p = 3$, where $\mathrm{sig}^q(x) = |x|^q \,\mathrm{sgn}(x)$.

(3). Power-sigmoid activation function: $\phi_{\mathrm{ps}}(x) = \begin{cases} \mathrm{sig}^{q_s}(x), & |x| \geq 1, \\ \dfrac{1+\exp(-\zeta)}{1-\exp(-\zeta)} \dfrac{1-\exp(-\zeta x)}{1+\exp(-\zeta x)}, & |x| < 1, \end{cases}$ where $q_s = 3$ and $\zeta = 2$.

(4). Sign-bi-power activation function (Li et al. [25]): $\phi_{\mathrm{sbp}}(x) = 1/2\,\mathrm{sig}^{\mu}(x) + 1/2\,\mathrm{sig}^{1/\mu}(x)$, where $\mu = 0.5$.

(5). Adapted ϕ_e-TGNN from Xie et al. [13]:

$$\phi_e(x) = \mu_1 \,\mathrm{sig}^{\alpha}(x) + \mu_2(|x + c_e| - |x - c_e|) + \mu_3 \,\mathrm{sig}^{\delta}(x),$$

where

$$\mu_1, \mu_2, \mu_3 > 0, \qquad 0 < \alpha < 1, \qquad \delta > 1, \qquad c_e > 0.$$

Unlike the preceding models, this activation function is applied to the PSTE residual before the adjoint mapping. Its adapted periodic tensor dynamics are given by

$$\dot{\mathcal{X}}_j(t) = -\gamma\Big[\mathcal{A}_j^{\mathsf{T}} *_{\mathrm{N}} \Phi_e(\mathcal{E}_j(t)) + \Phi_e(\mathcal{E}_{j-1}(t)) *_M \mathcal{B}_{j-1}^{\mathsf{T}}\Big],$$

where $\Phi_e(\cdot)$ applies $\phi_e(\cdot)$ elementwise, and the periodic convention $\mathcal{E}_{-1}(t) = \mathcal{E}_{T-1}(t)$ is adopted.

Following the representative parameter setting reported in Xie et al. [13], the activation parameters are selected as

$$\mu_1 = \mu_2 = \mu_3 = 1, \qquad \alpha = 0.8, \qquad c_e = 10, \qquad \delta = 2.$$

All comparative models use identical coefficient tensors, exact solutions, initial tensor states, network gain, numerical integrator, simulation interval, and output time grid. The model adapted from Xie et al. [13] retains its original residual activation and adjoint mapping architecture rather than directly applying ϕ_e to the combined gradient.

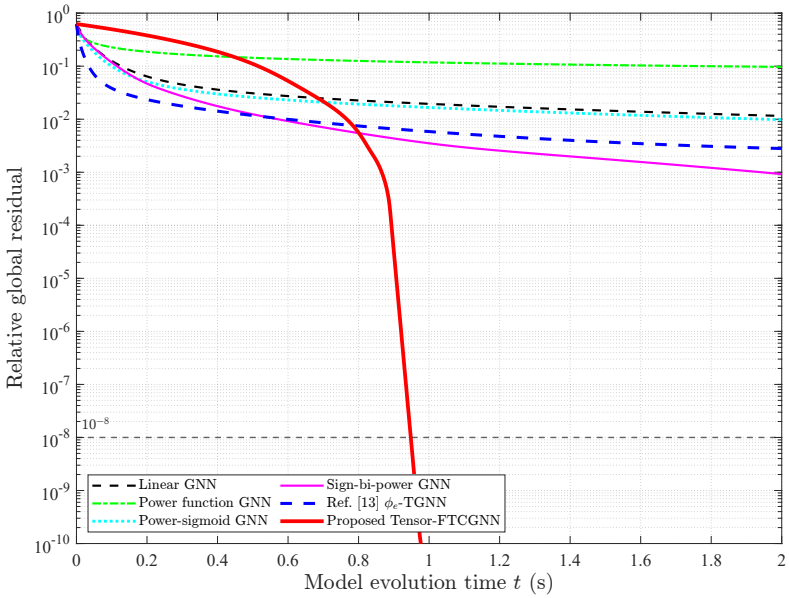

Figure 1. Convergence comparison of the relative global residual generated by the linear GNN, power-function GNN, power-sigmoid GNN, sign-bi-power GNN, the ϕ_e-TGNN adapted from Xie et al. [13], and the proposed regularized Tensor-FTCGNN. All models use the same PSTE coefficients, exact solutions, initial tensor states, network gain, numerical integrator, simulation interval, and output time grid. The horizontal dashed line denotes the prescribed relative residual tolerance of 10^{-8}.

It can be observed from Figure 1 that all comparative models reduce the relative global residual from the same initial value, but exhibit substantially different terminal convergence behaviors. Within the simulation interval $t \in [0, 2]$, the linear, power, power-sigmoid, sign-bi-power, and adapted ϕ_e-TGNN models do not reach even the relative residual level of 10^{-4}, and hence do not attain the prescribed tolerance of 10^{-8} shown in Figure 1.

Among these comparative models, the sign-bi-power GNN obtains the smallest terminal relative residual, 9.2463×10^{-4}. The adapted ϕ_e-TGNN from Xie et al. [13] reaches a final relative residual of 2.7988×10^{-3}. The final residuals of the power-sigmoid and linear GNNs are 9.8031×10^{-3} and 1.1533×10^{-2}, respectively, whereas the power-function GNN reaches 9.6918×10^{-2} under the adopted parameter setting. In contrast, the proposed regularized Tensor-FTCGNN initially produces a smooth decrease of the residual and subsequently exhibits a sharp terminal reduction.

Under the adopted parameter settings, the proposed global norm-based adaptive mechanism produces a faster terminal residual reduction than the tested element wise activation models for the periodically coupled PSTE considered in this experiment.

Because the numerical implementation employs the regularization parameter ϵ, the observed trajectory should be interpreted as finite-time entrance into an ϵ-dependent high-accuracy region followed by exponential refinement. This result is consistent with the two-phase convergence property established for the regularized model.

To reduce the dependence on a single random instance, ten independent trials are conducted using seeds 101–110. In each trial, the PSTE coefficients and initial states are regenerated, and all methods use the same instance and the numerical settings of Figure 1. The column "Reached 10^{-4}" records the number of trials for which the relative global residual satisfies $r_{\mathrm{rel}}(t) \le 10^{-4}$ within $t \in [0, 2]$; the time statistics are computed only over those trials.

Table 2. Multiple-trial comparison over ten independent PSTE instances.

Method	Terminal residual (mean ± std)	Reached 10^{-4}	Time to 10^{-4} (s)
Linear GNN	$1.375 \times 10^{-2} \pm 4.076 \times 10^{-3}$	0/10	–
Power-function GNN	$1.044 \times 10^{-1} \pm 2.330 \times 10^{-2}$	0/10	–
Power-sigmoid GNN	$1.164 \times 10^{-2} \pm 3.226 \times 10^{-3}$	0/10	–
Sign-bi-power GNN	$2.233 \times 10^{-3} \pm 9.792 \times 10^{-4}$	0/10	–
Adapted ϕ_e-TGNN	$5.020 \times 10^{-3} \pm 2.173 \times 10^{-3}$	0/10	–
Proposed Tensor-FTCGNN	$1.619 \times 10^{-5} \pm 3.612 \times 10^{-5}$	9/10	0.9972 ± 0.1282

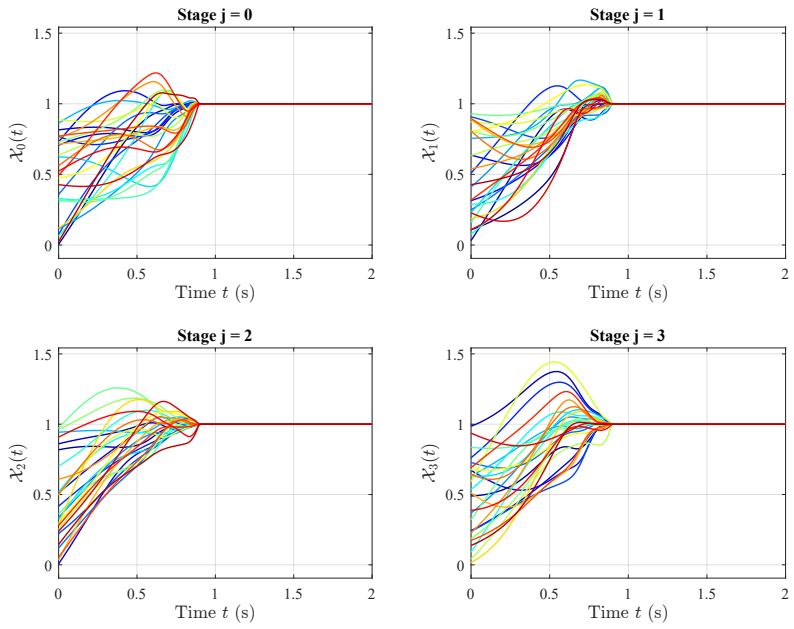

Figure 2. Trajectories of all 27 elements of the 3rd-order tensor states $\mathcal{X}_j(t), (j = 0, 1, 2, 3)$ across four stages. All elements converge simultaneously to the prescribed exact value of 1, demonstrating the simultaneous convergence of the periodically coupled tensor states.

As shown in Table 2, the proposed Tensor-FTCGNN reaches 10^{-4} by $t = 2$ in nine of the ten trials, while the remaining trial terminates at 1.062×10^{-4}. No numerical solver failure occurs.

To further illustrate the state evolution, Figure 2 displays the trajectories of all 27 elements of each third-order tensor state over the four periodic stages. Despite starting from random initial values, all tensor elements converge consistently toward the prescribed theoretical value of 1. The simultaneous alignment of the state trajectories confirms the successful solution of the four periodically coupled tensor equations considered in this test.

4.2. Quantitative verification of the Phase I entrance-time bound

To evaluate the conservativeness of the Phase I entrance-time bound in Proposition 3.5, we compare its predicted upper bound with the observed entrance time of the regularized Tensor-FTCGNN. Under the present setting $p = 1$, the regularized dynamics coincide with the ideal continuous-time dynamics whenever $\Omega(t)^{p/2} > \epsilon$. Therefore, the residual-based estimate derived in Theorem 3.2 also provides a conservative upper bound for the time required to enter the regularization region $\mathcal{D}_\epsilon$.

Using the residual-based estimate in Theorem 3.2, the Phase I entrance-time bound can be written as

$$T_{\max} = \frac{\lambda_{\max}^p \|\mathcal{E}(0)\|_{\mathbb{H}}^p}{p\gamma\lambda_{\min}^{1+p/2}} = \frac{C_T \|\mathcal{E}(0)\|_{\mathbb{H}}^p}{\gamma}, \tag{4.1}$$

where

$$C_T = \frac{\lambda_{\max}^p}{p\lambda_{\min}^{1+p/2}}. \tag{4.2}$$

Here, $\lambda_{\min}$ and $\lambda_{\max}$ denote the smallest and largest eigenvalues of the normal operator $\mathscr{H} = \mathscr{L}^*\mathscr{L}$, respectively.

For this experiment, an independent reproducible PSTE instance is constructed to permit direct evaluation of the spectral quantities in (4.1). We set $n = 3$, $T = 4$, and prescribe $\mathcal{X}_j^* = \mathbf{1}_{3\times3\times3}$, $j = 0, 1, 2, 3$. The left coefficient matrices and the auxiliary right coefficient matrices are generated as

$$A_j = Q_{A,j}\,\mathrm{diag}(1.8, 2.0, 2.2)Q_{A,j}^{\mathsf{T}} \tag{4.3}$$

and

$$\widehat{B}_j = Q_{B,j}\,\mathrm{diag}(0.15, 0.20, 0.25)Q_{B,j}^{\mathsf{T}}, \tag{4.4}$$

where $Q_{A,j}$ and $Q_{B,j}$ are orthogonal matrices obtained from QR factorizations of normally distributed random matrices. The fourth-order right coefficient tensor $\mathcal{B}_j$ is represented implicitly through $\widehat{B}_j$ using the same structured construction described in Section 4.1. The target tensors are then constructed from the prescribed exact solution according to the PSTE. The entries of the initial tensor states $\mathcal{X}_j(0)$ are independently sampled from the uniform distribution on $(-1, 1)$. The same initial tensor states are used for all three gain values. The random seed is fixed at 42.

Under the Frobenius norm-preserving vectorization described in Remark 2.5, the combined periodic operator is represented by L_{mat}, and $H_{\mathrm{mat}} = L_{\mathrm{mat}}^{\mathsf{T}} L_{\mathrm{mat}}$. Therefore,

$$\lambda_{\min} = \sigma_{\min}^2(L_{\mathrm{mat}}), \qquad \lambda_{\max} = \sigma_{\max}^2(L_{\mathrm{mat}}), \tag{4.5}$$

and the condition number of the combined operator is

$$\kappa_{\mathscr{L}} = \frac{\sigma_{\max}(L_{\mathrm{mat}})}{\sigma_{\min}(L_{\mathrm{mat}})} = \sqrt{\frac{\lambda_{\max}}{\lambda_{\min}}}. \tag{4.6}$$

The computed spectral quantities are listed in Table 3.

Table 3. Spectral characteristics of the combined periodic operator used in the Phase-I entrance-time experiment.

$\sigma_{\min}(L_{\mathrm{mat}})$	$\sigma_{\max}(L_{\mathrm{mat}})$	$\lambda_{\min}$	$\lambda_{\max}$	$\kappa_{\mathscr{L}}$
1.625695	2.354192	2.642884	5.542219	1.448114

For this instance, the coefficient in (4.2) is $C_T = 1.289932$, and the initial global residual is $\|\mathcal{E}(0)\|_{\mathbb{H}} = 27.216032$. The regularized Tensor-FTCGNN is tested with

$$p = 1, \qquad \epsilon = 10^{-4}, \qquad \gamma \in \{15, 30, 45\}.$$

The simulations are performed in MATLAB R2023b using `ode15s`, with RelTol = 10^{-6}, AbsTol = 10^{-6}. Because`ode15s` is an adaptive variable-step solver, no fixed internal integration step is imposed. The numerical solutions are reported on the common output grid

$$t_k = 10^{-3}k, \qquad k = 0, 1, \ldots, 3000,$$

over the interval $t \in [0, 2.5]$.

For each gain, the Phase I entrance time is defined by

$$t_\epsilon = \inf\left\{t \geq 0 : \Omega(t)^{p/2} \leq \epsilon\right\}. \tag{4.7}$$

The value of t_ϵ is located using the event-detection function of `ode15s`, rather than being estimated from the first reported output sample satisfying the threshold. The resulting entrance times and theoretical upper bounds are reported in Table 4.

Table 4. Observed Phase I entrance times and theoretical upper bounds for different network gains.

γ	t_ϵ (s)	$T_{\max}$ (s)	$t_\epsilon/T_{\max}$	$\|\mathcal{E}(t_\epsilon)\|_{\mathbb{H}}$
15	0.845428	2.340455	0.361224	6.073×10^{-5}
30	0.422714	1.170227	0.361224	6.071×10^{-5}
45	0.281809	0.780152	0.361224	6.071×10^{-5}

As shown in Figure 3 and Table 4, the observed Phase I entrance times are 0.845428 s, 0.422714 s, and 0.281809 s for $\gamma = 15$, 30, and 45, respectively. The corresponding theoretical upper bounds are 2.340455 s, 1.170227 s, and 0.780152 s. Hence,

$$t_\epsilon < T_{\max}$$

holds for all three tested gains.

Because the operator, initial state, and regularization parameter are kept unchanged, both t_ϵ and $T_{\max}$ decrease in inverse proportion to γ. Their ratio remains approximately

$$\frac{t_\epsilon}{T_{\max}} = 0.361224,$$

showing that the theoretical estimate is conservative but valid for this representative instance.

After entering the ϵ-dependent region, the residual decreases rapidly to a numerical floor, consistent with the Phase II exponential convergence established in Proposition 3.5. Nevertheless, the primary purpose of this experiment is to verify the Phase I entrance-time bound rather than to estimate the Phase II decay rate. The results show that the event-located entrance times of the regularized Tensor-FTCGNN satisfy the conservative upper bound inherited from the ideal model analysis for this representative reproducible instance.

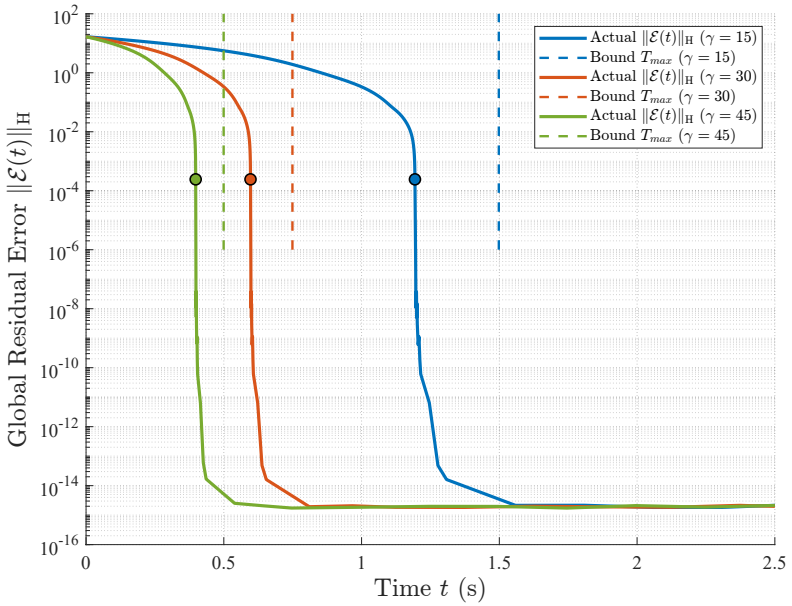

Figure 3. Comparison of the observed Phase I entrance times with the theoretical finite-time upper bounds. The solid curves denote the global residual norms $\|\mathcal{E}(t)\|_{\mathbb{H}}$ under different network gains γ, and the vertical dashed lines denote the corresponding theoretical upper bounds $T_{\max}$. The marked points indicate the observed entrance times t_ϵ into the regularized region.

4.3. Dimension-dependent numerical performance

In modern engineering applications, such as high-resolution image processing and large-scale multiagent systems, data are frequently represented in high-dimensional tensor forms. Therefore, it is important to investigate how the convergence behavior of the proposed neurodynamic model changes as the tensor dimension increases.

To examine this issue, the proposed regularized Tensor-FTCGNN is tested on PSTEs with

$$n \in \{5, 10, 15\}.$$

The total number of scalar unknowns in the periodically coupled system is Tn^3 and therefore increases cubically with n. The coefficient matrices and their structured right-operator representations are generated in the same manner as in Section 4.1.

For all tested dimensions, we set $T = 4$, $\gamma = 100$, $p = 1, \epsilon = 10^{-6}$, and use the simulation interval $t \in [0, 3]$.

For the structured third-order implementation, each left or right mode multiplication requires $O(n^4)$ arithmetic operations. Because a fixed number of such tensor products is evaluated at each of the T periodic stages, one right-hand-side evaluation requires $O(Tn^4)$ operations.

The overall algorithmic storage required by the tensor states, residuals, gradients, and structured coefficient data is $O(Tn^3)$. The full block matrix representation of the periodic operator is not assembled. This storage estimate excludes the internal workspace of the adaptive ordinary differential equation (ODE) solver, which depends on the MATLAB implementation and computing platform.

Figure 4 shows the global residual trajectories for the three tensor dimensions. As the dimension increases, the initial residual generally becomes larger, and the convergence rate decreases. For $n = 5$ and $n = 10$, the residual decreases below the displayed vertical range; the corresponding terminal values are reported in Table 5. For the larger case $n = 15$, the residual continues to decrease throughout the simulation interval, but does not reach the same accuracy level as the lower-dimensional cases within $t \in [0, 3]$.

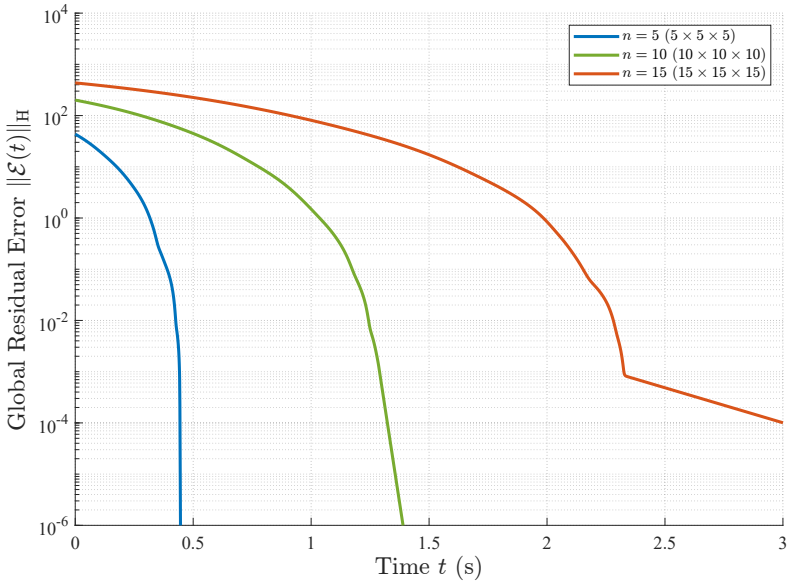

Figure 4. Global residual trajectories of the proposed regularized Tensor-FTCGNN for increasing tensor dimensions $n = 5$, 10, and 15. The residual decreases for all tested mode sizes, and the convergence becomes slower as the size of the coupled dynamical system increases.

Table 5. Single-run dimension-dependent numerical performance of the structured Tensor-FTCGNN implementation.

n	Scalar states Tn^3	Solver runtime (s)	Terminal residual
5	500	2.189	5.025×10^{-15}
10	4000	301.590	4.783×10^{-13}
15	13,500	4096.881	1.006×10^{-4}

The reported runtimes correspond to one representative solver run for each dimension and include only the call to the ODE solver; residual postprocessing and figure generation are excluded. Therefore, the reported wall clock times should be regarded as implementation- and platform-dependent references rather than hardware-independent benchmarks.

As shown in Table 5, the structured implementation attains terminal residuals below 10^{-12} for $n = 5$ and $n = 10$. For $n = 15$, the residual continues to decrease but reaches only 1.006×10^{-4} within the prescribed simulation interval. The substantial increase in solver runtime and the reduced terminal accuracy for $n = 15$ indicate that the computational cost remains strongly dimension dependent.

Therefore, these results should be interpreted as an assessment of dimension-dependent numerical performance over the tested sizes, rather than as evidence of dimension-independent scalability.

4.4. Application to cooperative periodic trajectory reconstruction of multiarm robotic systems

To illustrate the use of the proposed PSTE framework in periodically coupled multiarm trajectory reconstruction, we consider a cooperative system consisting of three robotic arms performing repetitive spatial tasks. The present study focuses on the trajectory-reference reconstruction layer: Prescribed periodic Cartesian samples are embedded into coupled tensor states, and the Tensor-FTCGNN is used to recover the corresponding periodic state sequence from randomly initialized tensor states.

The reconstructed Cartesian trajectories may subsequently serve as reference inputs to a lower-level inverse kinematic or feedback control module. The design of such a downstream controller is not considered in the present work.

In applications such as synchronized painting, cyclic assembly, and automated scanning, multiple robotic arms may be required to follow prescribed periodic spatial trajectories. The prescribed periodic trajectories of the three robotic arms are discretized into T stages and represented by third-order tensor states. The resulting periodically coupled reconstruction problem is formulated as the following PSTE:

$$\mathcal{A}_j *_N \mathcal{X}_j + \mathcal{X}_{j+1} *_M \mathcal{B}_j = C_j, \qquad j = 0, 1, \ldots, T-1,$$

subject to the periodic condition $\mathcal{X}_T = \mathcal{X}_0$. For the three-arm numerical example, we adopt $N = 1$, $M = 2$, and $n = 3$, so that $\mathcal{X}_j, C_j \in \mathbb{R}^{3\times3\times3}$. The first mode indexes the three robotic arms, whereas the second mode corresponds to the three Cartesian coordinates. The first slice along the third mode is used to encode the spatial trajectory displayed in Figure 5, namely

$$(\mathcal{X}_j)_{\ell,1,1} = x_{\ell,j}, \qquad (\mathcal{X}_j)_{\ell,2,1} = y_{\ell,j}, \qquad (\mathcal{X}_j)_{\ell,3,1} = z_{\ell,j}$$

for $\ell = 1, 2, 3$.

The coefficient matrices $\mathcal{A}_j$ and the auxiliary matrices $\widehat{B}_j$ are generated as symmetric positive-definite matrices to obtain a well-conditioned periodically coupled operator. The prescribed reference

tensors $\{\mathcal{X}_j^*\}_{j=0}^{T-1}$ are constructed from the desired periodic trajectories, and the corresponding target tensors are generated by

$$\mathcal{C}_j = \mathcal{A}_j *_1 \mathcal{X}_j^* + \mathcal{X}_{j+1}^* *_2 \mathcal{B}_j.$$

This construction provides a controlled model-based benchmark in which the reconstruction accuracy can be directly evaluated against a known reference.

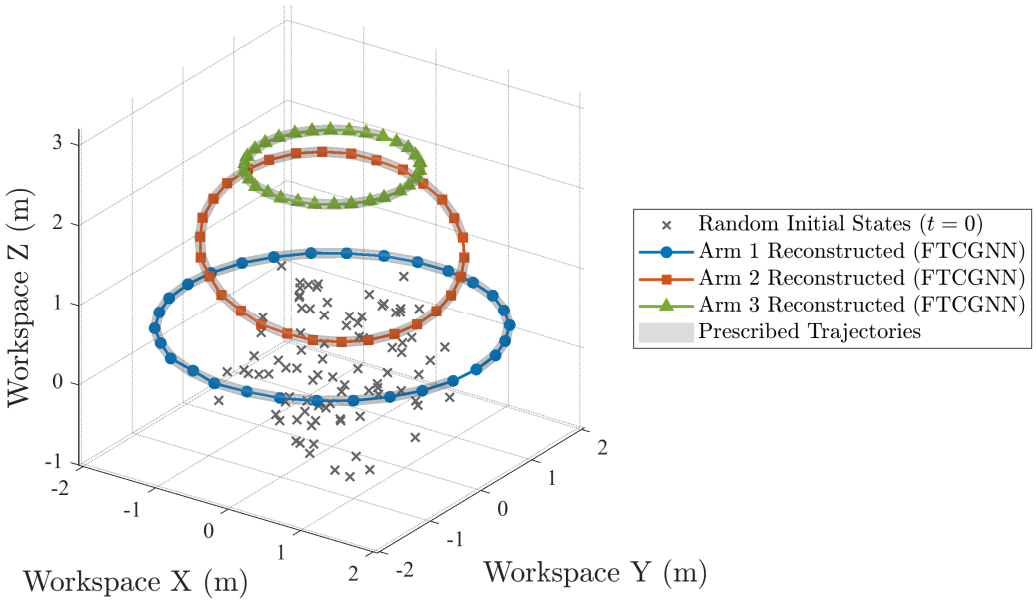

Figure 5. Cooperative periodic trajectory reconstruction for a three-arm robotic system using the proposed Tensor-FTCGNN. The gray crosses denote the randomly initialized tensor states, the translucent tubes represent the prescribed Cartesian reference trajectories, and the colored curves denote the reconstructed periodic trajectories at the final model evolution time.

The proposed regularized Tensor-FTCGNN is employed to solve the resulting periodically coupled tensor equation. Figure 5 illustrates the reconstructed periodic spatial trajectories of the three robotic arms. For each stage j, the Cartesian coordinates of the ℓth arm are extracted from the first third-mode slice of the reconstructed tensor state as

$$((\mathcal{X}_j)_{\ell,1,1}, (\mathcal{X}_j)_{\ell,2,1}, (\mathcal{X}_j)_{\ell,3,1}).$$

The gray crosses denote the corresponding coordinate components of the randomly initialized tensor states, the translucent tubes represent the prescribed periodic trajectories, and the colored curves show the reconstructed trajectories obtained from the final Tensor-FTCGNN state.

The close agreement between the prescribed and reconstructed trajectories shows that the proposed Tensor-FTCGNN successfully recovers the periodically coupled Cartesian reference sequence from

randomly initialized tensor states. The reconstructed curves preserve the periodicity and spatial coordination of the three reference trajectories and exhibit no visible numerical chattering in the reported simulation.

The reconstructed trajectories can subsequently be interpreted as Cartesian reference signals for inverse kinematic or motion control processing.

4.4.1. Sampling interval sensitivity of the piecewise-constant Jacobian approximation

The preceding experiment evaluates the reconstruction of periodic Cartesian reference trajectories within the PSTE framework. When such reference trajectories are subsequently used in a sampled robotic kinematic implementation, an additional approximation may arise if the configuration-dependent Jacobian is held constant over each sampling interval.

We therefore conduct a separate sensitivity study to quantify this implementation-related approximation.

For this sensitivity study, the motion of the ℓth robotic arm is described by the standard differential kinematic model $\dot{\boldsymbol{r}}_\ell(t) = \boldsymbol{J}_\ell(\boldsymbol{q}_\ell(t))\dot{\boldsymbol{q}}_\ell(t)$, where $\boldsymbol{q}_\ell(t)$ denotes the joint configuration vector, and $\boldsymbol{r}_\ell(t)$ denotes the corresponding end-effector position. The Jacobian matrix is obtained from the forward kinematic mapping $\boldsymbol{r}_\ell = \boldsymbol{f}_\ell(\boldsymbol{q}_\ell)$ as

$$\boldsymbol{J}_\ell(\boldsymbol{q}_\ell) = \frac{\partial \boldsymbol{f}_\ell(\boldsymbol{q}_\ell)}{\partial \boldsymbol{q}_\ell}.$$

The joint trajectories $\boldsymbol{q}_\ell(t)$ are prescribed as smooth and bounded motion profiles over the simulation horizon. The same kinematic parameters, joint trajectories, and initial configurations are used for all tested sampling intervals, so that the reported deviations reflect only the approximation error introduced by freezing the Jacobian.

Here, $\boldsymbol{q}(t)$ denotes the stacked joint-configuration vector of the multiarm system, t_k is the beginning of the kth sampling interval, and $\Delta\tau > 0$ denotes the sampling interval. The Jacobian is evaluated at t_k and kept fixed over $[t_k, t_k + \Delta\tau)$.

Remark 4.1. Suppose that the robotic Jacobian is locally Lipschitz continuous, such that

$$\|\mathcal{J}(q_1) - \mathcal{J}(q_2)\| \le L_J \|q_1 - q_2\|$$

for admissible configurations q_1 and q_2, where $L_J > 0$ denotes a local Lipschitz constant. Assume further that

$$\|\dot{q}(t)\| \le V_{\max},$$

where $V_{\max} > 0$ is an upper bound on the joint velocity. Consequently, the instantaneous velocity-mapping error caused by freezing the Jacobian satisfies

$$\left\| [\mathcal{J}(\boldsymbol{q}(t)) - \mathcal{J}(\boldsymbol{q}(t_k))]\, \dot{\boldsymbol{q}}(t) \right\| \le L_J V_{\max}^2 \Delta\tau.$$

Thus, the instantaneous approximation error is $O(\Delta\tau)$, the local position error over one interval is $O(\Delta\tau^2)$, and the accumulated error over a fixed time horizon is expected to be $O(\Delta\tau)$.

The sensitivity study is conducted for

$$\Delta\tau \in \{0.001, 0.002, 0.005, 0.01, 0.02\}\ \text{s},$$

using identical kinematic parameters, joint-motion profiles, initial configurations, and simulation horizons for all tested sampling intervals. Let N_s denote the number of sampled time instants. For the ℓth robotic arm at the kth sample, $r_{\ell,k}$ and $\bar{r}_{\ell,k}$ denote the end-effector positions generated by the continuously varying nonlinear Jacobian model and the piecewise-constant Jacobian model, respectively, where $\ell = 1, \ldots, L$, and $k = 1, \ldots, N_s$.

The RMS and maximum end-effector approximation deviations are defined as

$$e_{\mathrm{RMS}} = \sqrt{\frac{1}{LN_s} \sum_{\ell=1}^{L} \sum_{k=1}^{N_s} \left\| \boldsymbol{r}_{\ell,k} - \widehat{\boldsymbol{r}}_{\ell,k} \right\|_2^2},$$

and

$$e_{\max} = \max_{\ell,k} \left\| \boldsymbol{r}_{\ell,k} - \widehat{\boldsymbol{r}}_{\ell,k} \right\|_2 .$$

As shown in Figure 6, both e_{RMS} and $e_{\max}$ increase approximately linearly with $\Delta\tau$, which is consistent with the predicted $O(\Delta\tau)$ accumulated error. Under the selected accuracy requirement $\eta = 10^{-2}$ m, all tested sampling intervals up to $\Delta\tau = 0.01$ s satisfy $e_{\max} \leq \eta$. When $\Delta\tau = 0.02$ s, the maximum deviation increases to 1.3117×10^{-2} m and exceeds the prescribed requirement. This sampling limit characterizes the piecewise-constant Jacobian approximation under the selected kinematic setting and is not a convergence condition of the Tensor-FTCGNN itself.

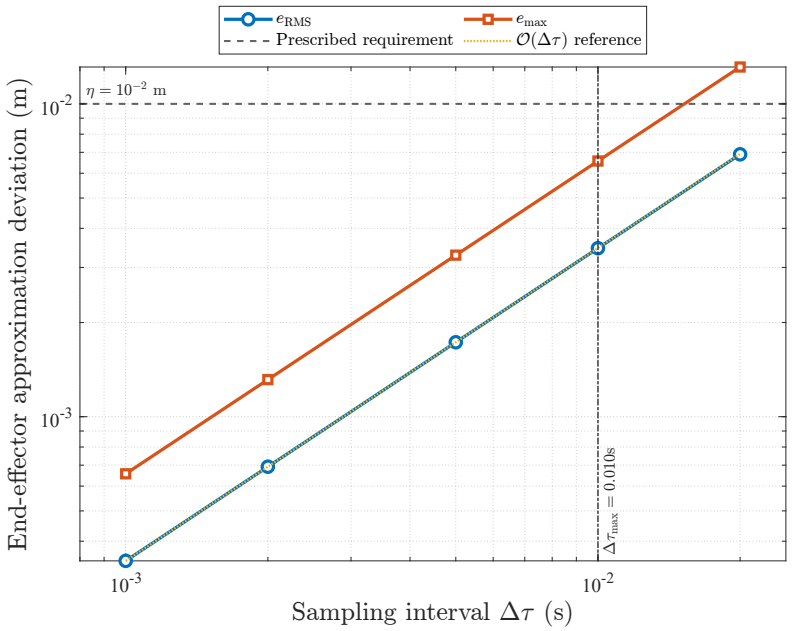

Figure 6. Sensitivity of the piecewise-constant Jacobian approximation to the sampling interval $\Delta\tau$. The RMS and maximum end-effector approximation deviations increase approximately linearly with $\Delta\tau$. The horizontal dashed line denotes the selected accuracy requirement $\eta = 10^{-2}$ m, and the vertical dash-dotted line indicates the maximum tested admissible sampling interval $\Delta\tau_{\max} = 0.01$ s.

Therefore, the maximum tested admissible sampling interval is

$$\Delta\tau_{\max} = 0.01 \text{ s},$$

corresponding to a sampling frequency of 100 Hz. This value is specific to the robot parameters, motion profiles, simulation horizon, and accuracy requirement considered in this experiment, rather than a universal sampling limit.

The two experiments address complementary aspects of the proposed application framework. Figure 5 evaluates the recovery of periodically coupled Cartesian reference trajectories through the PSTE solver, whereas Figure 6 quantifies the sampling error that may arise in a subsequent piecewise-constant Jacobian kinematic implementation. A fully integrated measurement, inverse kinematic, and closed-loop control system remains beyond the scope of the present study.

5. Conclusions

In this paper, a class of periodic Sylvester tensor equations was formulated as a unified linear operator equation on a product tensor space, and a Tensor-FTCGNN with a global adaptive gain was developed. Under the unique solvability condition, the ideal continuous-time model was proved to converge globally to the exact PSTE solution within a finite time, together with an explicit settling-time upper bound. For numerical implementation, the regularized model was shown to reach an ϵ-dependent high-accuracy region in finite time and subsequently converge exponentially to the exact solution. Numerical experiments compared the proposed regularized model with representative GNN models, examined its performance over multiple independent PSTE instances, and confirmed that the observed Phase I entrance times remained below the corresponding theoretical upper bounds. The dimension-dependent experiments further characterized the convergence behavior, runtime, and computational cost over the tested tensor sizes. Finally, the multiarm robotic example demonstrated the use of the proposed framework for periodically coupled trajectory-reference reconstruction, and a separate sampling interval sensitivity study quantified the approximation error associated with a piecewise-constant Jacobian.

Future work will extend the proposed framework to time-varying PSTEs and broader tensor equations, including generalized Sylvester, Lyapunov, Riccati, and coupled tensor–matrix equations. Robust neurodynamic models will also be investigated for systems subject to noise, coefficient perturbations, and external disturbances. In addition, low-rank tensor, tensor-train, and dictionary-based representations will be incorporated to reduce the storage and computational costs of large-scale PSTEs. Parallel and distributed implementations on multicore processors and GPUs, and experimental validation on physical multiarm robotic platforms, will be considered in future studies.

Use of AI tools declaration

The authors declare they have not used Artificial Intelligence (AI) tools in the creation of this article.

Author Contributions

All authors contributed equally to the conceptualization, formal analysis, investigation, methodology, software, validation, writing of the original draft, writing of the review, and editing. All authors have read and agreed to the published version of the manuscript.

Acknowledgments

This work was supported by the National Natural Science Foundation of China under Grant No. 12301028.

Conflict of interest

Yang Zhang is a guest editor for [Electronic Research Archive] and was not involved in the editorial review or the decision to publish this article. All authors declare that there are no competing interests.

References

1. Z. H. He, A. Dmytryshyn, Q. W. Wang, A new system of Sylvester-like matrix equations with arbitrary number of equations and unknowns over the quaternion algebra, *Linear Multilinear Algebra*, **73** (2025), 1269–1309. https://doi.org/10.1080/03081087.2024.2413635
2. Z. H. He, L. W. Ye, Y. Z. Xu, M. L. Deng, QSVD method for arbitrary multiple Sylvester-type coupled quaternion matrix equations with applications, *Comput. Appl. Math.*, **45** (2026), 155. https://doi.org/10.1007/s40314-025-03488-1
3. T. Li, Q. W. Wang, X. F. Duan, Numerical algorithms for solving discrete Lyapunov tensor equation, *J. Comput. Appl. Math.*, **370** (2020), 112676. https://doi.org/10.1016/j.cam.2019.112676
4. Q. W. Wang, X. Xu, X. F. Duan, Least squares solution of the quaternion Sylvester tensor equation, *Linear Multilinear Algebra*, **69** (2021), 104–130. https://doi.org/10.1080/03081087.2019.1588848
5. M. Xie, Q. W. Wang, Y. Zhang, The BiCG algorithm for solving the minimal Frobenius norm solution of generalized Sylvester tensor equation over the quaternions, *Symmetry*, **16** (2024), 1167. https://doi.org/10.3390/sym16091167
6. L. Lv, J. Chen, L. Zhang, F. Zhang, Gradient-based neural networks for solving periodic Sylvester matrix equations, *J. Franklin Inst.*, **359** (2022), 10849–10866. https://doi.org/10.1016/j.jfranklin.2022.05.023
7. S. Li, C. Ma, An improved gradient neural network for solving periodic Sylvester matrix equations, *J. Franklin Inst.*, **360** (2023), 4056–4070. https://doi.org/10.1016/j.jfranklin.2023.02.019
8. A. G. Wu, W. X. Zhang, Y. Zhang, An iterative algorithm for discrete periodic Lyapunov matrix equations, *Automatica*, **87** (2018), 395–403. https://doi.org/10.1016/j.automatica.2017.06.012
9. S. Bittanti, P. Colaneri, *Periodic Systems: Filtering and Control*, Springer, London, 2009. https://doi.org/10.1007/978-1-84800-911-0

10. S. Hara, Y. Yamamoto, T. Omata, M. Nakano, Repetitive control system: A new type servo system for periodic exogenous signals, *IEEE Trans. Autom. Control*, **33** (1988), 659–668. https://doi.org/10.1109/9.1274

11. T. G. Kolda, B. W. Bader, Tensor decompositions and applications, *SIAM Rev.*, **51** (2009), 455–500. https://doi.org/10.1137/07070111X

12. T. Li, Q. W. Wang, Structure preserving quaternion biconjugate gradient method, *SIAM J. Matrix Anal. Appl.*, **45** (2024), 306–326. https://doi.org/10.1137/23M1547299

13. M. Xie, Q. W. Wang, J. Chen, Fixed-time TGNN model with the nonlinear activation function for online solution of Sylvester tensor equation, *Numer. Algorithms*, **101** (2026), 1023–1047. https://doi.org/10.1007/s11075-025-02031-x

14. J. Xue, Y. Q. Zhao, T. Wu, J. C. W. Chan, Tensor convolution-like low-rank dictionary for high-dimensional image representation, *IEEE Trans. Circuits Syst. Video Technol.*, **34** (2024), 13257–13270. https://doi.org/10.1109/TCSVT.2024.3442295

15. Z. Qi, Y. Ning, L. Xiao, J. Luo, X. Li, Finite-time zeroing neural networks with novel activation function and variable parameter for solving time-varying Lyapunov tensor equation, *Appl. Math. Comput.*, **452** (2023), 128072. https://doi.org/10.1016/j.amc.2023.128072

16. C. Mo, D. Gerontitis, P. S. Stanimirović, Solving the time-varying tensor square root equation by varying-parameters finite-time Zhang neural network, *Neurocomputing*, **445** (2021), 309–325. https://doi.org/10.1016/j.neucom.2021.03.011

17. J. Li, X. Wang, K. Wang, Y. Wei, Neural networks for solving least squares solution of polynomial systems with time-varying tensors, *J. Comput. Appl. Math.*, **474** (2026), 116952. https://doi.org/10.1016/j.cam.2025.116952

18. L. Xiao, J. Hu, Q. Zuo, W. Kuang, L. Li, Nonlinear zeroing neural networks with lower upper bounds for time-varying algebraic tensor Riccati equation based on improper integral, *Neurocomputing*, **685** (2026), 133628. https://doi.org/10.1016/j.neucom.2026.133628

19. M. Xie, Q. W. Wang, Y. Zhang, An AF-CRP-enhanced zeroing neural network for time-varying generalized Sylvester matrix equations, *Neurocomputing*, **681** (2026), 133368. https://doi.org/10.1016/j.neucom.2026.133368

20. Y. Zhang, B. Liao, G. Geng, GNN model with robust finite-time convergence for time-varying systems of linear equations, *IEEE Trans. Syst. Man Cybern. Syst.*, **54** (2024), 4786–4797. https://doi.org/10.1109/TSMC.2024.3387023

21. M. D. Petković, M. Kostadinov, J. Dakić, Gradient neural dynamics for linear matrix equations and their applications, *Math. Comput. Simul.*, **249** (2026), 560–582. https://doi.org/10.1016/j.matcom.2026.05.031

22. J. Dakić, M. D. Petković, Gradient neural network model for the system of two linear matrix equations and applications, *Appl. Math. Comput.*, **481** (2024), 128930. https://doi.org/10.1016/j.amc.2024.128930

23. P. S. Stanimirović, M. D. Petković, Gradient neural dynamics for solving matrix equations and their applications, *Neurocomputing*, **306** (2018), 200–212. https://doi.org/10.1016/j.neucom.2018.03.058

24. A. Einstein, Die formale Grundlage der allgemeinen Relativitätstheorie, in *Albert Einstein: Akademie-Vorträge*, (1914), 1030–1085.

25. S. Li, S. Chen, B. Liu, Accelerating a recurrent neural network to finite-time convergence for solving time-varying Sylvester equation by using a sign-bi-power activation function, *Neural Process. Lett.*, **37** (2013), 189–205. https://doi.org/10.1007/s11063-012-9241-1

26. S. P. Bhat, D. S. Bernstein, Finite-time stability of continuous autonomous systems, *SIAM J. Control Optim.*, **38** (2000), 751–766. https://doi.org/10.1137/S0363012997321358

AIMS Press